Chapter 9
Mesoscopic Modelling of Strain Localization in Plain Concrete

Abstract. The Chapter deals with modelling of strain localization in concrete at meso-scale. Concrete was considered as a composite material by distinguishing three phases: cement matrix, aggregate and interfacial transition zones. For FE calculations, an isotropic damage model with non-local softening was used. The simulations were carried out with concrete specimens under uniaxial tension and bending. The effect of aggregate density, aggregate size, aggregate distribution, aggregate shape, aggregate stiffness, aggregate size distribution, characteristic length and specimen size was investigated. The representative volume element was also determined.

A mechanism of strain localization strongly depends upon a heterogeneous structure of materials over many different scales, which changes e.g. in concrete from the few nanometers (hydrated cement) to the millimetres (aggregate particles). Therefore, to take strain localization into account, material composition (micro-structure) has to be taken into account (Nielsen et al. 1995, Bažant and Planas 1998, Sengul et al. 2002, Lilliu and van Mier 2003, Du and Sun 2007, Kozicki and Tejchman 2008, He et al. 2009, Skarżyński and Tejchman 2010). At the meso-scale, concrete can be considered as a composite material by distinguishing three important phases: cement matrix, aggregate and interfacial transition zones ITZs. In particular, the presence of aggregate and ITZs is important since the volume fraction of aggregate can be as high as 70-75% in concrete and ITZs are always the weakest regions in concrete. The concrete behaviour at the meso-scale fully determines the macroscopic non-linear behaviour. The advantage of meso-scale modelling is the fact that it directly simulates micro-structure and can be used to comprehensively study local phenomena at the micro-level such as the mechanism of the initiation, growth and formation of localized zones and cracks (He 2010, Kim and Abu Al-Rub 2011, Shahbeyk et al. 2011). Through that the mesoscopic results allow for a better calibration of continuum models enhanced by micro-structure and an optimization design of concrete with enhanced strength and ductility. The disadvantages are: very high computational cost, inability to model aggregate shape accurately and the difficulty to experimentally measure the properties of ITZs. All FE

J. Tejchman, J. Bobiński: Continuous & Discontinuous Modelling of Fracture, SSGG, pp. 343–405.
springerlink.com

investigations of a heterogeneous three-phase concrete material at the meso-level encompassing cement matrix, aggregates and an interfacial transition zone (ITZ) between the cement matrix and aggregates were performed with an isotropic damage constitutive model with non-local softening using a Rankine failure type criterion to define the equivalent strain measure $\tilde{\varepsilon}$ (Eqs. 3.35-3.40). The inclusions were assumed to be mainly in a circular shape randomly distributed according to a sieve curve (Fig. 9.1) and embedded in a homogeneous cement matrix. There are two widely used methods for the generation of randomly situated aggregate inclusions. The first one allows one to obtain a dense packing of aggregates in two-dimensional body of concrete using a Fuller distribution (van Mier et al. 1995):

$$p = 100\sqrt{\frac{D}{D_{\max}}}, \tag{9.1}$$

where p is the percentage weight of particles passing a sieve with the diameter D and D_{max} is the size of a largest particle. Furthermore by using a cumulative distribution for a two-dimensional cross-section, the circle diameters for a concrete can be generated. The second method of particle generation used by Eckardt and Konke (2006) is more straightforward. First, a grading curve is chosen (based on experimental measurements). Next, the certain amounts of particles with defined diameters d_1, d_2 … d_n are generated according to this curve. In our book, the latter method was used. The circles were randomly placed in the prescribed area starting with the largest ones and preserving a certain mutual distance (van Mier et al. 1995):

$$D > 1.1\frac{D_1 + D_2}{2}, \tag{9.2}$$

where D is the distance between two neighbouring particle centers, and D_1 and D_2 are the diameters of two neighboring aggregate particles. In the next step, the generated particle structure was overlaid with an irregular mesh of triangles. The finite elements belonging to cement matrix, aggregate inclusions and bond zones, respectively, had own different properties. It was assumed that the inclusions and bond zones had the highest and the lowest stiffness, respectively (van Mier et al. 1995).

9.1 Uniaxial Tension

The properties of the cement matrix, aggregate inclusions and bond zones used for FE calculations using an isotropic damage model with non-local softening are shown in Tab. 9.1 (Skarżyński and Tejchman 2009). The size of inclusions varied from a_{min}=2.5 mm up to a_{max}=5 mm. The size of bond zone elements, 0.25 mm (equal to $0.1\times a_{min}$), was smaller than the size of cement matrix elements. The mesoscopic characteristic length of micro-structure was l_c=0.5 mm.

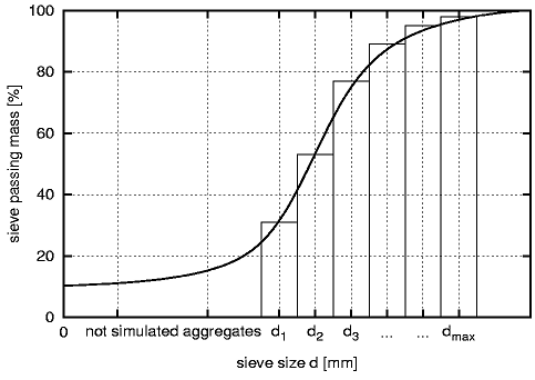

Fig. 9.1 Approximation of non-linear grading curve with discrete numbers of aggregate sizes (Skarżyński and Tejchman 2010)

Table 9.1 Material parameters assumed for uniaxial tension (Skarżyński and Tejchman 2009)

Material parameters	Inclusions	Cement matrix	ITZ
Modulus of elasticity E [GPa]	30	25	20
Poisson's ratio ν [-]	0.2	0.2	0.2
Crack initiation strain parameter κ_0 [-]	0.5	8×10^{-5}	5×10^{-5}
Residual stress level parameter α [-]	0.95	0.95	0.95
Slope of softening parameter β [-]	500	500	500

The calculations were carried out with periodic boundary conditions and material periodicity to avoid the effect of walls (van der Sluis 2001, Gitman 2006, Gitman et al. 2008). In the first case, the positions of nodes along corresponding specimen boundaries were the same before and after deformation. This is illustrated in Fig. 9.2, where an arbitrary periodically deformed unit cell under uniaxial extension conditions is shown. The deformation of each boundary pair is the same and the stresses are opposite in sign for each pair. The displacement boundary conditions are

$$u_{12} - u_4 = u_{11} - u_1 , \tag{9.3}$$

$$u_{22} - u_1 = u_{21} - u_2 , \tag{9.4}$$

$$u_3 - u_2 = u_2 - u_1 , \tag{9.5}$$

where u_{ij} is the displacement for any material point along the boundary Γ_{ij} and u_i is the node displacement. From the periodicity equations (Eqs. 9.3-9.5) can be observed that the independent entities are Γ_{11}, Γ_{21}, u_1, u_2 and u_4, whereas the tied dependent entities are Γ_{22}, Γ_{12} and u_3.

In addition, to eliminate wall effects, the periodicity of the material was assumed (Gitman 2006). Figure 9.3 presents samples different unit cells *A-F* in a concrete specimen. The cells *A, B, D* and *E* are valid in the context of material periodicity. However, the cells *C* and *F* experience wall-effects since some edges are crossed by inclusions. In our calculations, we avoided inclusions penetrating through the unit cell boundaries by letting them re-appear at the opposite edge (Fig. 9.4).

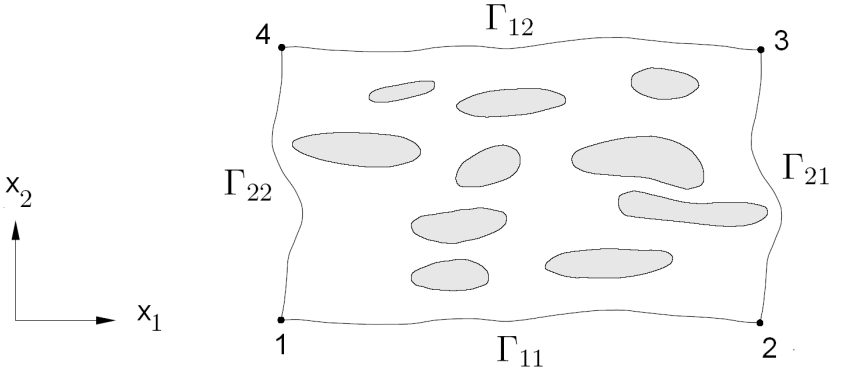

Fig. 9.2 Periodically deformed unit cell with boundaries Γ_R and nodes v_i (van der Sluis 2001)

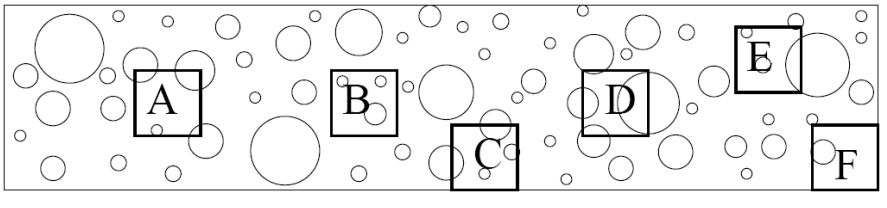

Fig. 9.3 Distribution of different unit cells in a concrete specimen (Gitman 2006)

A two-dimensional uniaxial tension test (Fig. 9.5) was performed with quadratic concrete specimens representing unit cells (Figs. 9.6-9.8) with periodicity of boundary conditions and material. For periodic boundary conditions, the displacements were suppressed in the node '*1*' (Fig. 9.2). Furthermore, in the node '*2*', a non-zero displacement was prescribed in a horizontal direction while the displacement a vertical direction was suppressed. The displacement components of the node '*3*' and '*4*' were free and tied together. The vertical normal stress was obtained from the resultant vertical force along the top

boundary divided by the cross-sectional area (B×1 m, where B is the width of the cell) and the strain as the vertical displacement of the top boundary divided by the cell width B.

First, concrete specimens of five different sizes were investigated. The smallest and the largest unit cells were 10×10 mm^2 and 25×25 mm^2, respectively (Fig. 9.6). For each specimen, five different stochastic realizations were performed (Fig. 9.7) with the aggregate density ρ kept constant (ρ=30%, ρ=45% and ρ=60%) (Fig. 9.8). Next, the calculations were carried out with a different characteristic length of micro-structure varying between l_c=0.1 mm-2.0 mm. Later, the effect of an aggregate density (ρ=30%, ρ=45% and ρ=60%) on strain localization was investigated. In the final comparative calculations, non-locality was prescribed to the cement matrix only.

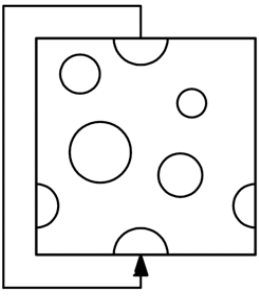

Fig. 9.4 Simulation of material periodicity (Gitman 2006)

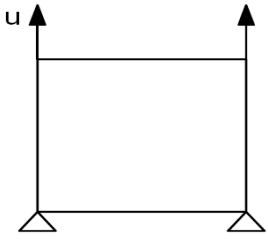

Fig. 9.5 Uniaxial tension test (Skarżyński and Tejchman 2009)

Effect of specimen size and realization

Figures 9.9-9.11 present the resultant mean macroscopic stress-strain relationships for various specimen sizes and random distributions of aggregate with the material constants from Tab. 9.1 (l_c=0.5 mm). The aggregate densities were ρ=30%, ρ=45% or ρ=60%, respectively. In turn, the influence of the specimen size on the evolution of the stress-strain curves for different aggregate densities is demonstrated in Fig. 9.12. The results evidently show that the stress-strain curves are the same independently of the specimen size, aggregate density and distribution of inclusions in an elastic regime only (almost up to the peak).

However, they are completely different in a softening regime after the peak is reached. An increase of the specimen size causes an increase of the material brittleness. The differences in the evolution of stress-strain curves in a softening regime are caused by strain localization contributing to a loss of the material homogeneity (Fig. 9.13). Strain localization in the form of a localized zone propagates between aggregates and can be strongly curved. The width of the calculated zone is about $w_c=(4\times l_c)=2$ mm (with $l_c=0.5$ mm).

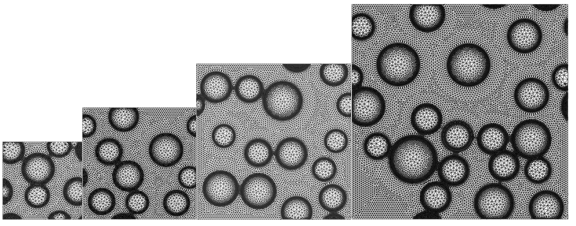

a) b) c) d)

Fig. 9.6 Different size of concrete specimens: a) 10×10 mm^2, b) 15×15 mm^2, c) 20×20 mm^2, d) 25×25 mm^2 (aggregate density ρ=30%) (Skarżyński and Tejchman 2009)

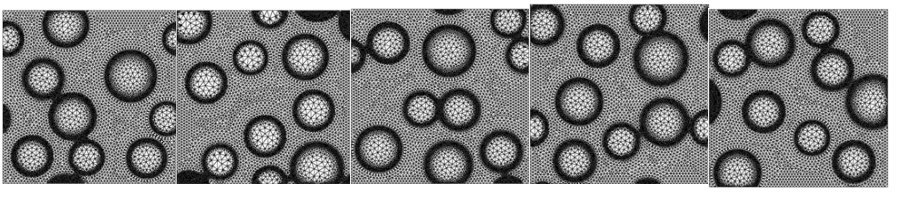

Fig. 9.7 Different stochastic distribution of aggregate for a concrete specimen of 15×15 mm^2 (aggregate density ρ=30%) (Skarżyński and Tejchman 2009)

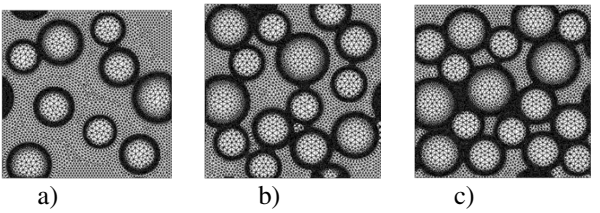

a) b) c)

Fig. 9.8 Different aggregate density ρ in concrete specimens: a) ρ=30%, b) ρ=45%, c) ρ=60% (Skarżyński and Tejchman 2009)

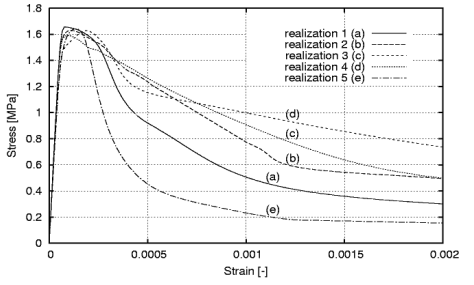

a)

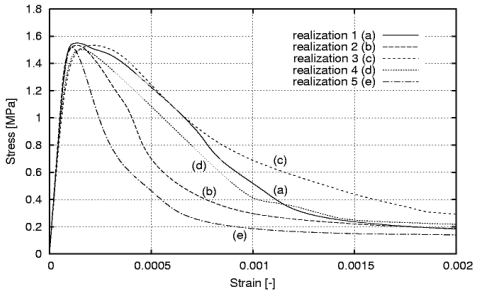

b)

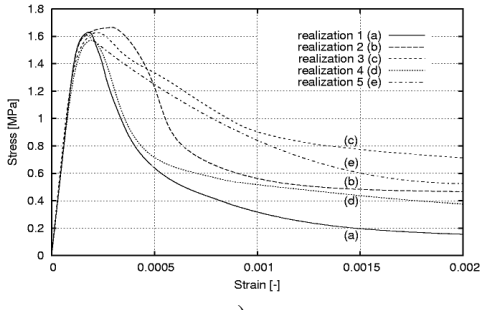

c)

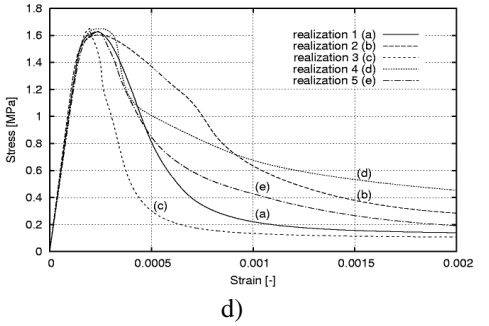

d)

Fig. 9.9 Stress-strain curves with various sizes of concrete specimen and random distributions of aggregates: a) 10×10 mm^2, b) 15×15 mm^2, c) 20×20 mm^2, d) 25×25 mm^2 (characteristic length l_c=0.5 mm, aggregate density ρ=30%) (Skarżyński and Tejchman 2009)

The results indicate that the RVE can be determined in a linear-elastic regime only (due to the lack of differences in the evolution of the stress-strain curves). However, it cannot be determined in a softening regime due to strain localization (Gitman et al. 2008).

Effect of characteristic length of micro-structure

The effect of a characteristic length of micro-structure on the stress-strain curve and strain localization is shown in Figs. 9.14-9.17. Figures 9.14 and 9.16 demonstrate the influence of l_c on the evolution of stress-strain curves with two different specimen sizes: 10×10 mm^2 and 25×25 mm^2, respectively. In turn, Figs. 9.15 and 9.17 present the distribution of a non-local softening strain measure for various l_c changing between 0.1 mm and 2.0 mm.

With increasing characteristic length, both specimen strength and width of a localized zone increase. On the other hand, softening decreases and material behaves more ductile. Thus, a pronounced size effect occurs. The width of a localized zone is about $w_c=4\times l_c$ independently of l_c. A localized zone propagating in a cement matrix between aggregates is strongly curved with l_c=0.25 mm-1.0 mm, whereas becomes more straight for l_c>1.0 mm (Fig. 9.17e).

Effect of aggregate density

Figure 9.18 demonstrates the effect of the aggregate density on the stress-strain curves for two specimen sizes: 20×20 mm^2 and 25×25 mm^2, respectively (ρ=30%, ρ=45% or ρ=60% with l_c=0.5 mm).

A localized zone is also influenced by aggregate spacing. With increasing aggregate density, a localized zone becomes slightly narrower (Fig. 9.19). This means that a characteristic length of micro-structure may not be related to the aggregate size only but also to the grain size of the cement matrix.

Effect of non-locality range

Figure 9.20 shows the influence of the range of non-locality on the stress-strain relationship. In contrast to above studies, where non-locality was prescribed to all 3 phases of concrete, here, a cement matrix was solely assumed to be non-local due to fact that strain localization occurred only there. A characteristic length was again 0.5 mm.

The effect of the non-locality range on results turned out to be insignificant since the range of averaging slightly decreased (Figs. 9.20 and 9.21).

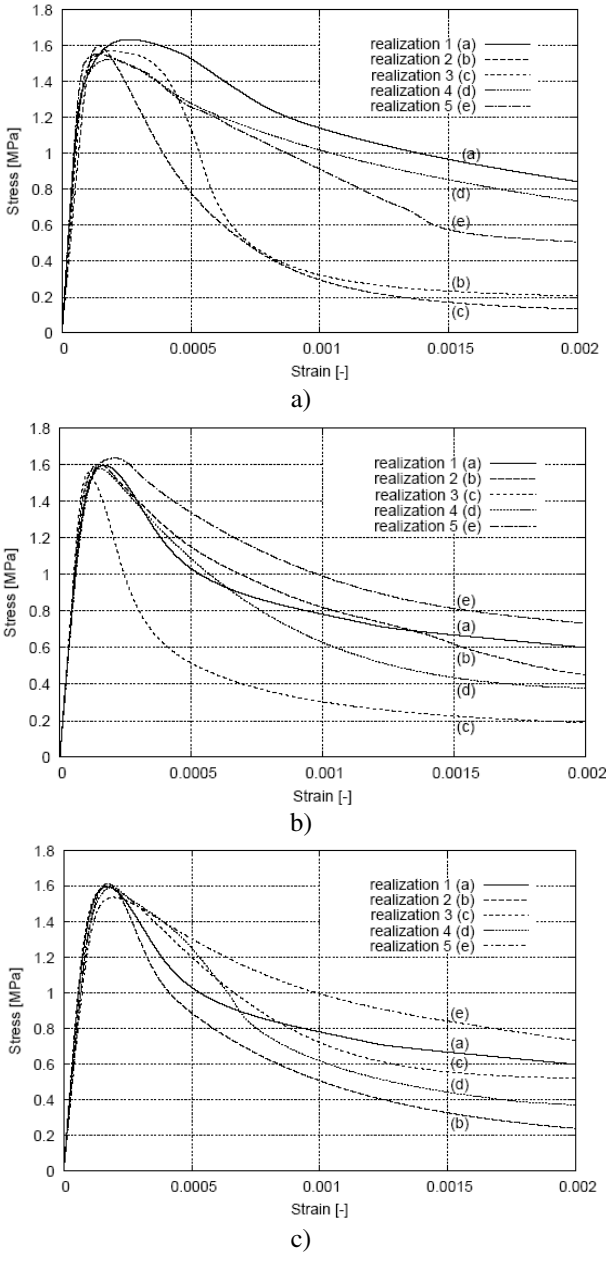

Fig. 9.10 Stress-strain curves for various sizes of concrete specimens and random distributions of aggregates: a) 10×10 mm^2, b) 15×15 mm^2, c) 20×20 mm^2, d) 25×25 mm^2 (characteristic length l_c=0.5 mm, aggregate density ρ=45%) (Skarżyński and Tejchman 2009)

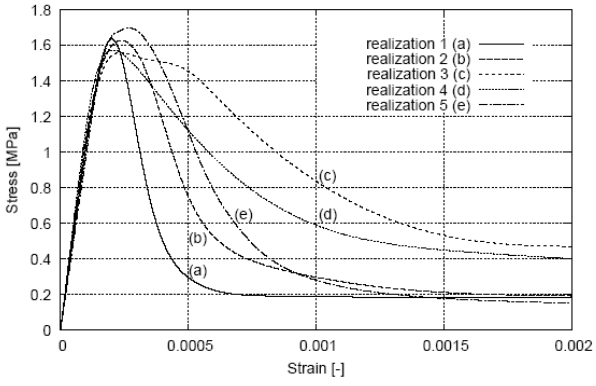

d)

Fig. 9.10 (*continued*)

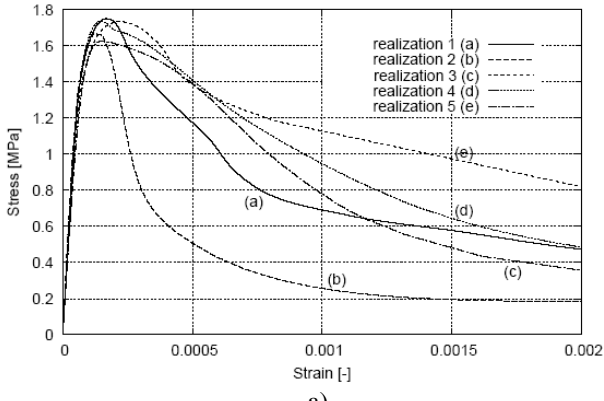

a)

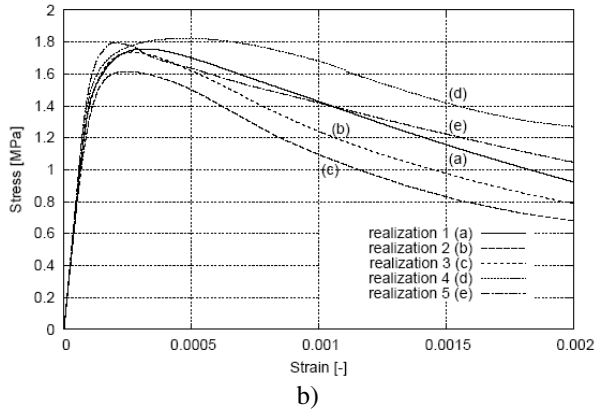

b)

Fig. 9.11 Stress-strain curves for various sizes of concrete specimens and random distributions of aggregates: a) 10×10 mm^2, b) 15×15 mm^2, c) 20×20 mm^2, d) 25×25 mm^2 (characteristic length l_c=0.5 mm, aggregate density ρ=60%) (Skarżyński and Tejchman 2009)

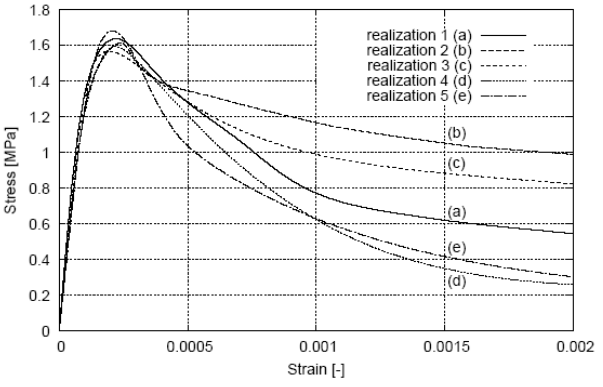

c)

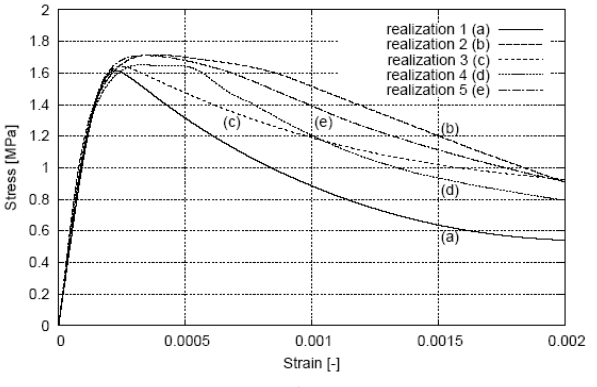

d)

Fig. 9.11 (*continued*)

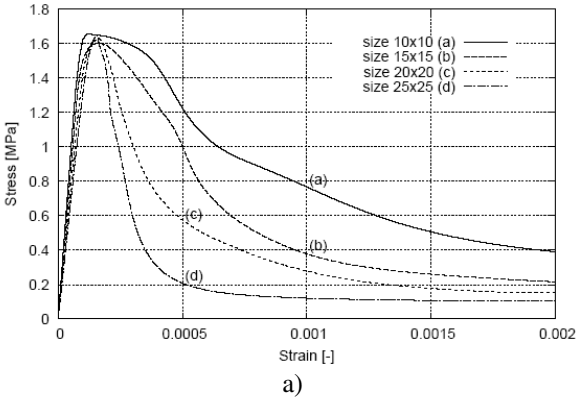

a)

Fig. 9.12 Stress-strain curves for various sizes specimen sizes of concrete specimens and aggregate densities ρ: a) ρ=30%, b) ρ=45%, c) ρ=60% (characteristic length l_c=0.5 mm) (Skarżyński and Tejchman 2009)

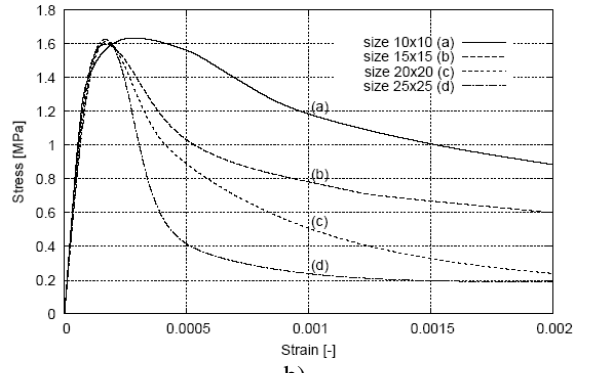

b)

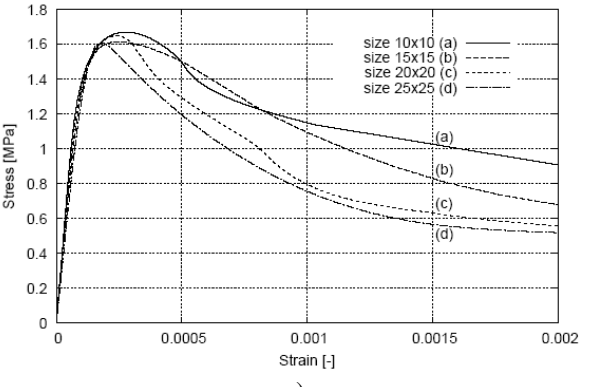

c)

Fig. 9.12 (*continued*)

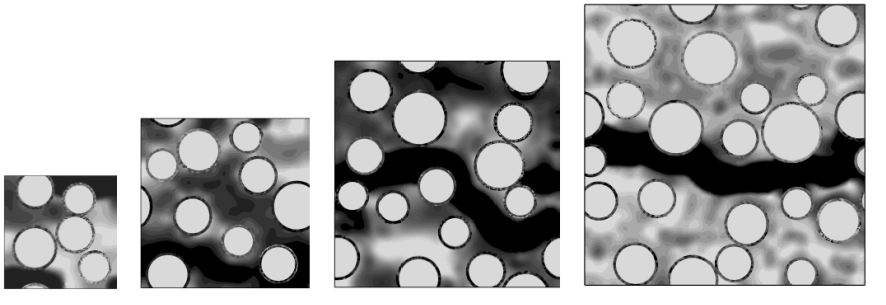

Fig. 9.13 Distribution of non-local strain measure for different specimen sizes with two different stochastic realizations of aggregate density: a) 10×10 mm^2, b) 15×15 mm^2, c) 20×20 mm^2, d) 25×25 mm^2 (characteristic length l_c=0.5 mm, aggregate density ρ=30%) (Skarżyński and Tejchman 2009)

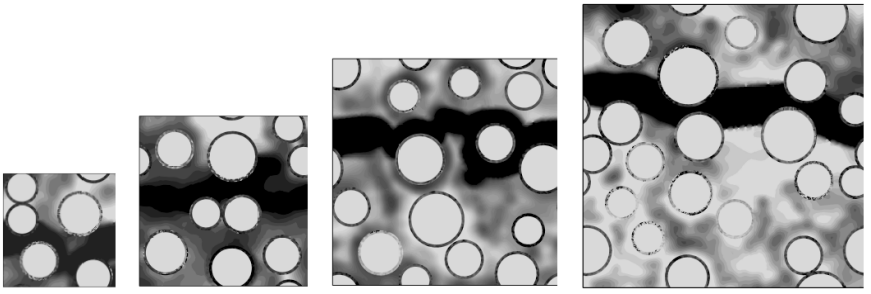

Fig. 9.13 (*continued*)

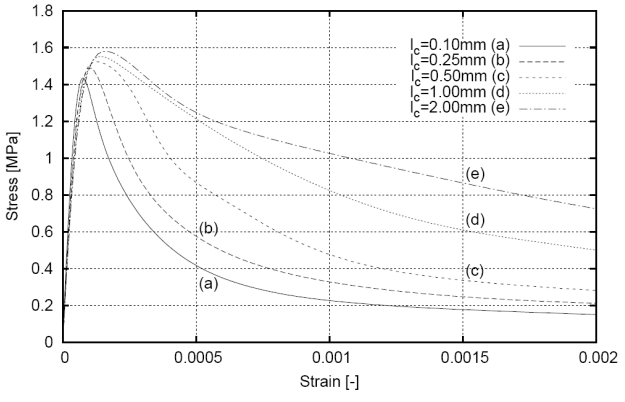

Fig. 9.14 Stress-strain curves for different characteristic lengths: a) l_c=0.1 mm, b) l_c=0.25 mm, c) l_c=0.5 mm, d) l_c=1.0 mm, e) l_c=2.0 mm (specimen size 10×10 mm^2, aggregate density ρ=30%) (Skarżyński and Tejchman 2009)

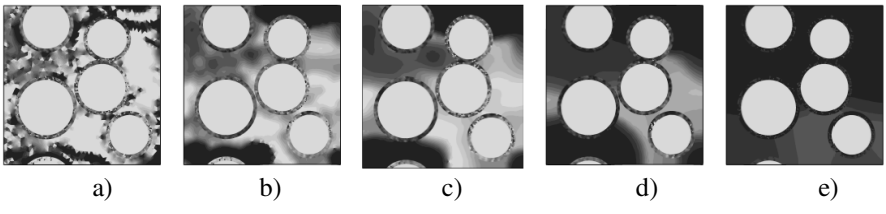

Fig. 9.15 Distribution of non-local softening strain measure for different characteristic lengths l_c: a) l_c=0.1 mm, b) l_c=0.25 mm, c) l_c=0.5 mm, d) l_c=1.0 mm, e) l_c=2.0 mm (specimen size 10×10 mm^2, aggregate density ρ=30%) (Skarżyński and Tejchman 2009)

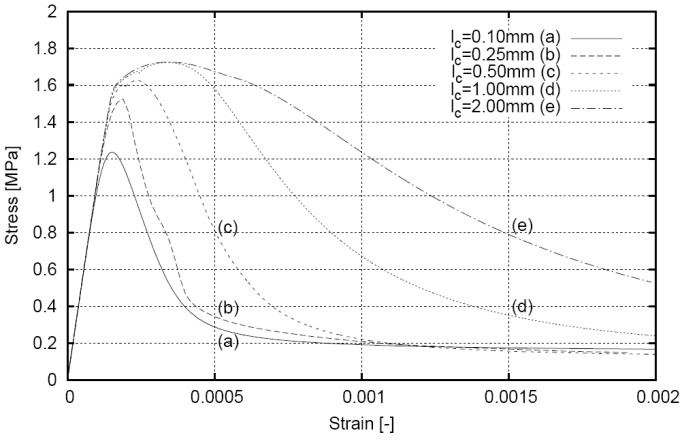

Fig. 9.16 Stress-strain curves for different values of a characteristic length: a) l_c=0.1 mm, b) l_c=0.25 mm, c) l_c=0.5 mm, d) l_c=1.0 mm, e) l_c=2.0 mm (specimen size 25×25 mm^2, aggregate density ρ=30%) (Skarżyński and Tejchman 2009)

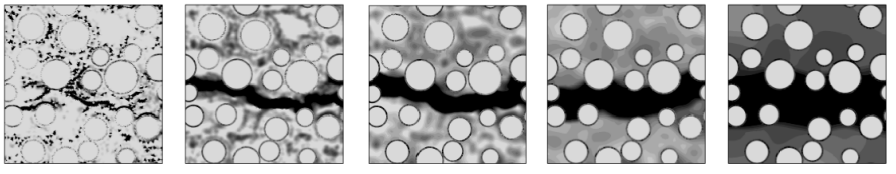

Fig. 9.17 Distribution of non-local softening strain measure for different values of a characteristic length: a) l_c=0.1 mm, b) l_c=0.25 mm, c) l_c=0.5 mm, d) l_c=1.0 mm, e) l_c=2.0 mm (specimen size 25×25 mm^2, aggregate density ρ=30%) (Skarżyński and Tejchman 2009)

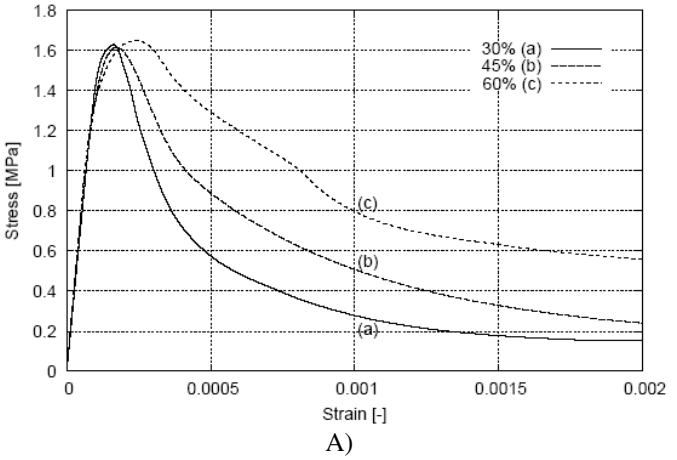

Fig. 9.18 Stress-strain curves for aggregate densities: (a) ρ=30%, (b) ρ=45%, (c) ρ=60% and cell sizes: (A) 20×20 mm^2 (B) 25×25 mm^2 (l_c=0.5 mm) (Skarżyński and Tejchman 2009)

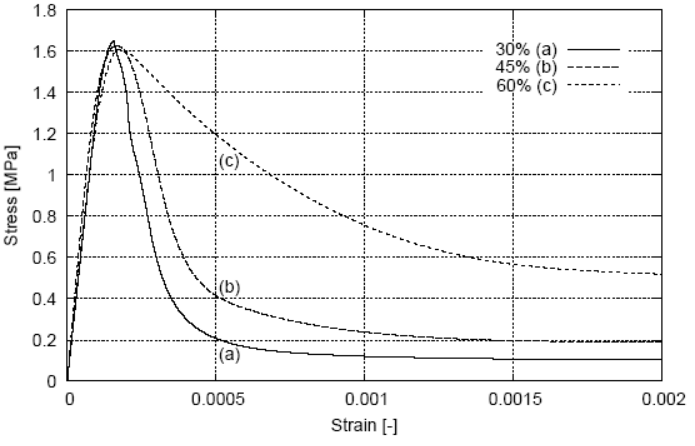

B)

Fig. 9.18 (*continued*)

9.2 Bending

If the meso-structure of concrete is taken into account, such FE modeling is connected with a very large number of finite elements. To solve the problem practically, a macro-meso connection is used. It is done in a direct way, where a region with strain localization is considered at the meso-scale and a remaining region at the macro-level using a constitutive model. Alternatively, a computational homogenization is made using a multi-scale approach (Gitman et al. 2008, Geers et al. 2010, Kaczmarczyk et al. 2010). In this approach, the macro-meso connection is used as a constitutive equation on the macro-level. Thus, instead of an explicit formulation of the stress-strain relation, the data from the meso-level is taken into account. The idea of such technique is as follows: the strain from the macro-level goes in the form of boundary conditions to the meso-level, where a heterogeneous material behaviour is modeled, after which the reaction forces to boundary conditions are transformed by means of a homogenization technique (by changing the macro-level constitutive tangent stiffness) as stresses back to the macro-level. Different models for concrete can be used at meso-scale, e.g. discrete (interface element models (Carol et al. 2001), lattice approaches (Kozicki and Tejchman 2008), discrete element models DEM (Donze at al. 1999)) or continuum models (with cohesive elements (Kaczmarczyk et al. 2010), enhanced by a characteristic length of micro-structure (Gitman et al. 2008) or using displacement discontinuities (Belytschko et al. 2001, 2009).

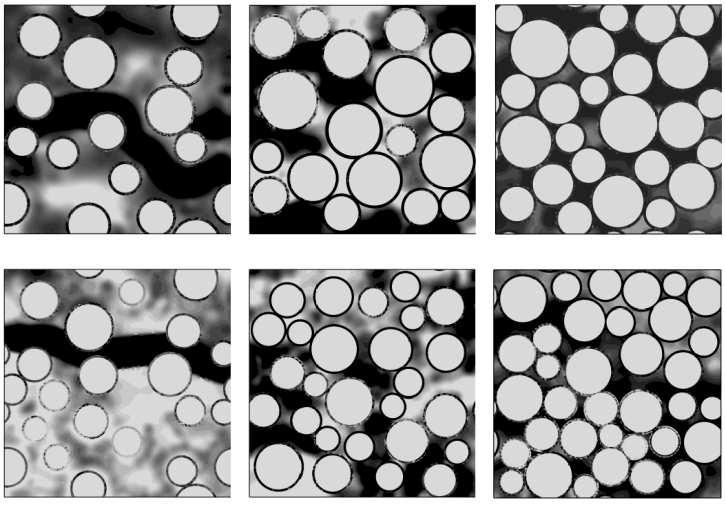

Fig. 9.19 Distribution of non-local softening strain measure for different aggregate densities: a) ρ=30%, b) ρ=45%, c) ρ=60% and specimen sizes: A) 20×20 mm^2, B) 25×25 mm^2 (l_c=0.5 mm) (Skarżyński and Tejchman 2009)

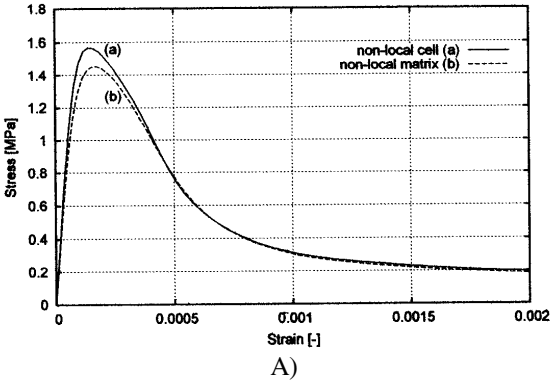

Fig. 9.20 Stress-strain curves for 2 different specimen sizes: A) 15×15 mm^2, B) 25×25 mm^2 with a) non-locality prescribed to three phases and b) non-locality prescribed to cement matrix (aggregate density ρ=30%, characteristic length l_c=0.5 mm) (Skarżyński and Tejchman 2009)

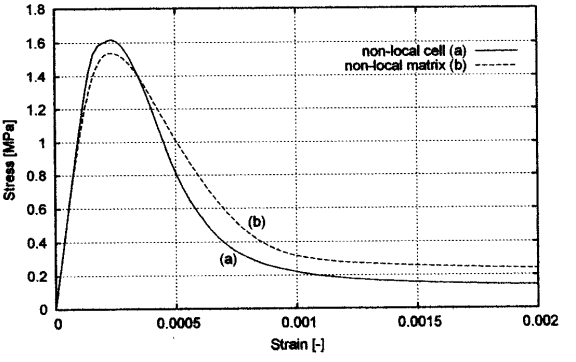

B)

Fig. 9.20 (*continued*)

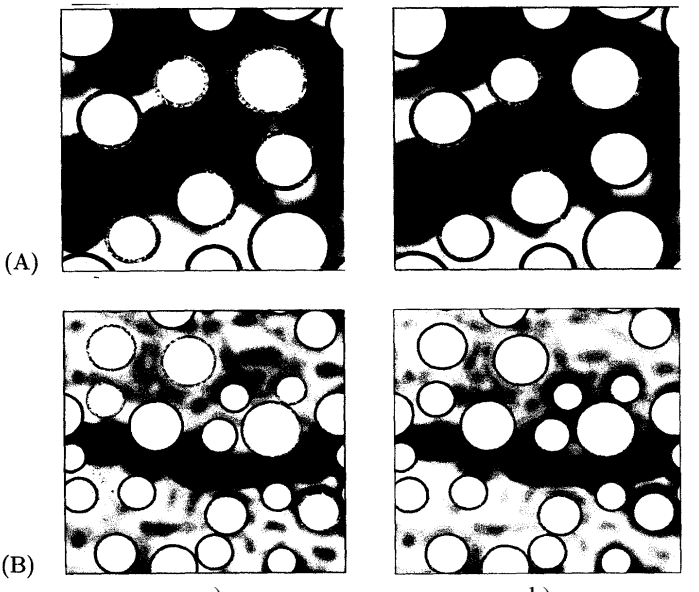

Fig. 9.21 Distribution of non-local softening strain measure for 2 different specimen sizes: A) 15×15 mm^2, B) 25×25 mm^2 with a) non-locality prescribed to three phases and b) non-locality prescribed to cement matrix (aggregate density ρ=30%, characteristic length l_c=0.5 mm) (Skarżyński and Tejchman 2009)

Experiments

The three-point bending laboratory tests were carried out with concrete beams of a different size $D \times L$ (D - beam height, $L=4 \times D$ - beam length) with free ends (Skarzyński et al. 2011), Fig. 9.22a. The beams were geometrically similar in two dimensions only for 2 reasons: a) to reduce the number of finite elements and the

related computation time in FE calculations at meso-scale (two-dimensional analyses were carried out instead of three-dimensional ones) and b) to avoid differences in the hydration heat effects which are proportional to the thickness of the member (Bažant and Planas, 1998). The following concrete beams were used: a) small-size beams 80×320 mm^2, b) medium-size beams 160×640 mm^2 and c) large-size beams 320×1280 mm^2 (Fig. 9.22a). The thickness of beams was always the same b=40 mm, and the beams' span was equal to 3×D. A notch with a height of D/10 mm was located at the mid-span of the beam bottom. The beams were subjected to a vertical displacement in the mid-point at a very slow rate. Two different fine-grained concrete mixes were composed of ordinary Portland cement, water and fine sand (with a mean aggregate diameter d_{50}=0.5 mm and maximum aggregate diameter d_{max}=3.0 mm) or sand (d_{50}=2.0 mm, d_{max}=8.0 mm) (Fig. 9.22b). The width and shape of a localized zone above the notch on the surface of beams was determined with a Digital Image Correlation (DIC) method which is an optical way to visualize surface displacements by successive post-processing of

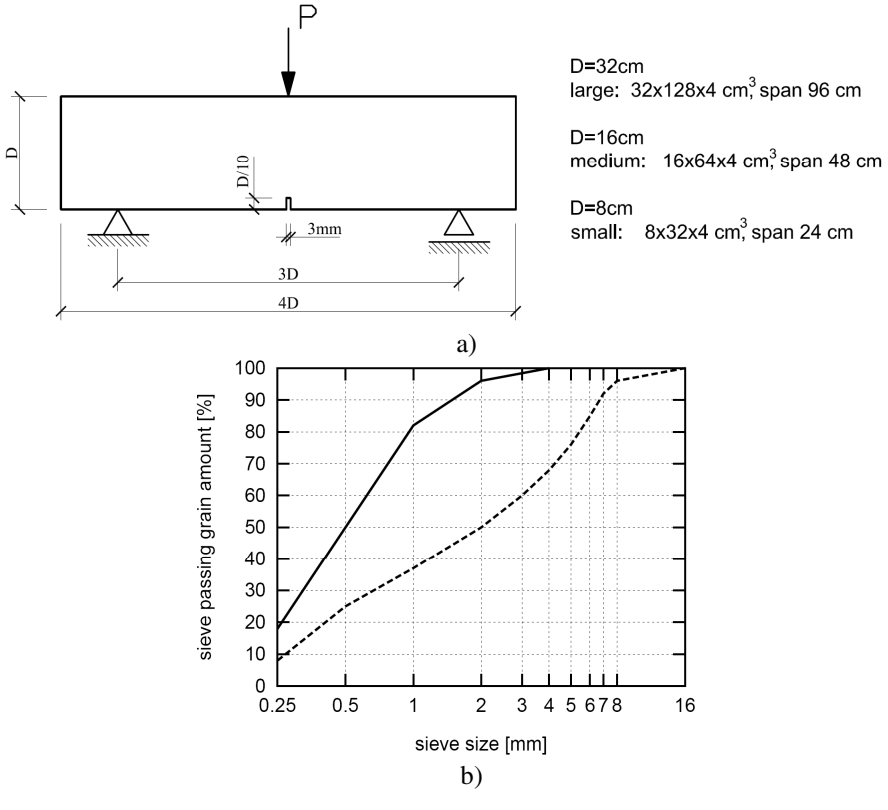

Fig. 9.22 Geometry of experimental concrete beams subjected to three-point bending: a) geometry (Le Bellĕgo et al. 2003, Skarżyński et al. 2011), b) grading curve for fine sand (continuous line) and sand (discontinuous line) used for concrete (Skarżyński et al. 2011)

digital images taken at a constant time increment from a professional digital camera (based on displacements, strains can be calculated) (White et al. 2003). The experimental set-up and results were described in detail by Skarżyński et al. (2011). The beams of the same size were also used by Le Bellĕgo et al. (2003).

Figure 9.23 shows the formation of a localized zone on one side of the surface of a fine-grained small-size concrete beam above the notch from laboratory tests

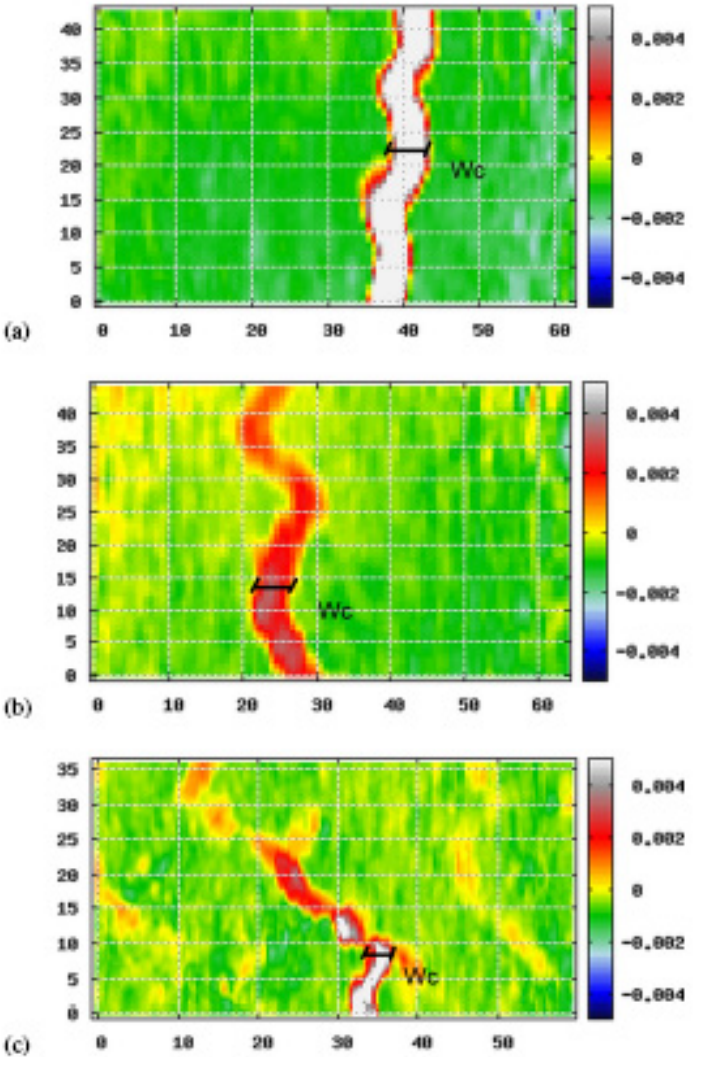

Fig. 9.23 Formation of localized zone with mean width of w_c=3.5-4.0 mm directly above notch in 3 different experiments ('a', 'b' and 'c') with small-size notched fine-grained concrete beam 80×320×40 mm^3 using DIC (vertical and horizontal axes denote coordinates in [mm] and colour scales strain intensity) (Skarżyński et al. 2011)

using a DIC (Skarżyński et al. 2011). A localized zone occurred always before the peak on the force-deflection diagram and was strongly curved. In some cases, it branched. The measured width of a localized zone above the notch increased during deformation due to concrete dilatancy (Fig. 9.24A) up to w_c=3.5-4.0 mm ($\leq d_{max}$) in the range of the deflection u=0.01-0.04 mm until a macro-crack was created. The maximum height of a localized zone above the notch was about h_c=50-55 mm at u=0.04 mm (Fig. 9.24B). The width of a localized zone did not depend upon the concrete mix type and beam size (Skarżyński et al. 2011).

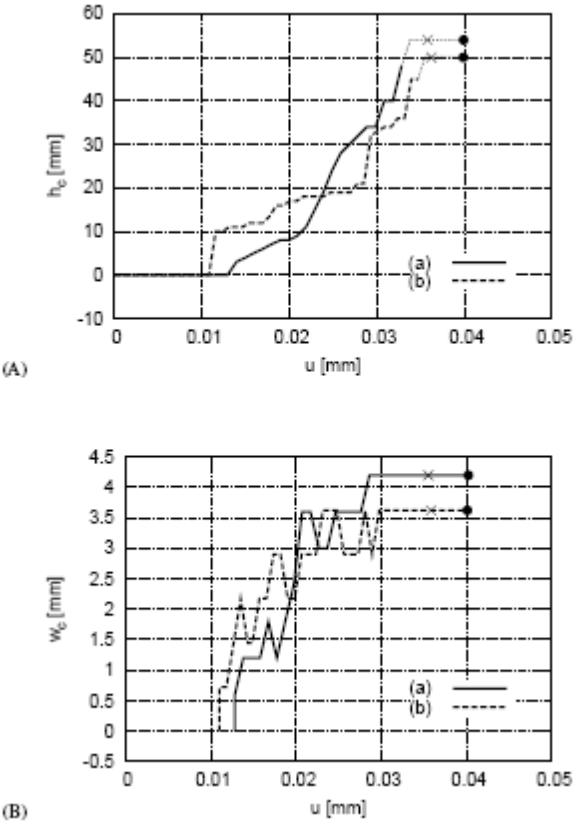

Fig. 9.24 Evolution of width w_c (A) and height h_c (B) of localized zone with deflection u directly above notch in experiments with small-size notched beam 80×320×40 mm^3 of fine-grained concrete using DIC: a) aggregate d_{50}=2 mm and d_{max}=8 mm, b) aggregate d_{50}=0.5 mm and d_{max}=3 mm (× - maximum vertical force, • - formation of macro-crack) (Skarżyński et al. 2011)

FE results

The FE-meshes including 12'000-1'600'000 triangular elements were assumed (Skarżyński and Tejchman 2010). The calculations were carried out with one set of material parameters for usual concrete only which was prescribed to finite

elements corresponding to a specified concrete phase (Tab. 9.2) using an isotropic damage model with non-local softening. The interface was again assumed to be the weakest component. In general, the material constants should be determined through laboratory tensile tests for each phase (that is certainly possible for aggregate and cement matrix but not feasible for ITZs). Since the material constants for aggregate and cement matrix were not separately determined with laboratory experiments, other relationships between material constants E and κ_0 were also possible to obtain a satisfactory agreement between experiments and FE analyses.

Table 9.2 Material parameters assumed for three-point bending (Skarżyński and Tejchman 2010)

Material parameters	Inclusions	Cement matrix	Interface
Modulus of elasticity E [GPa]	40	35	30
Poisson's ratio ν [-]	0.2	0.2	0.2
Crack initiation strain parameter κ_o [-]	0.5	1×10^{-4}	7×10^{-5}
Residual stress level parameter α [-]	0.95	0.95	0.95
Slope of softening parameter β [-]	200	200	200

Four different fine-grained concrete mixes were numerically analysed (Fig. 9.25). To reduce the number of aggregate grains in calculations, the size of the smallest inclusions had to be limited (Fig. 9.25). The aggregate size varied between the minimum value d_{min}=2 mm and maximum value d_{max}=8 mm with the mean value of d_{50}=2 mm (aggregate size distribution curve '*a*' of Fig. 9.25 corresponding to the experimental one for sand concrete of Fig. 9.22b), d_{min}=2 mm and d_{max}=10 mm with d_{50}=4 mm (aggregate size distribution curve '*b*' of Fig. 9.25), d_{min}=2 mm and d_{max}=6 mm with d_{50}=4 mm (aggregate size distribution curve '*c*' of Fig. 9.25) and d_{min}=0.5 mm and d_{max}=3 mm with d_{50}=0.5 mm (aggregate size distribution curve '*d*' of Fig. 9.25 corresponding to the experimental one for fine sand concrete of Fig. 9.22b).

The width of ITZs was assumed to be t_b=0-0.75 mm. The size of finite elements was small enough to obtain objective results: s_a=0.5 mm (aggregate), s_{cm}=0.1-0.2 mm (cement matrix) and s_{ITZ}=0.05-0.1 mm (ITZ). The calculation time was about 2-5 days using PC with CPU Q6600 2×2.4 GHz and 4 GB RAM. The aggregate density was ρ=30%, ρ=45% or 60%, respectively.

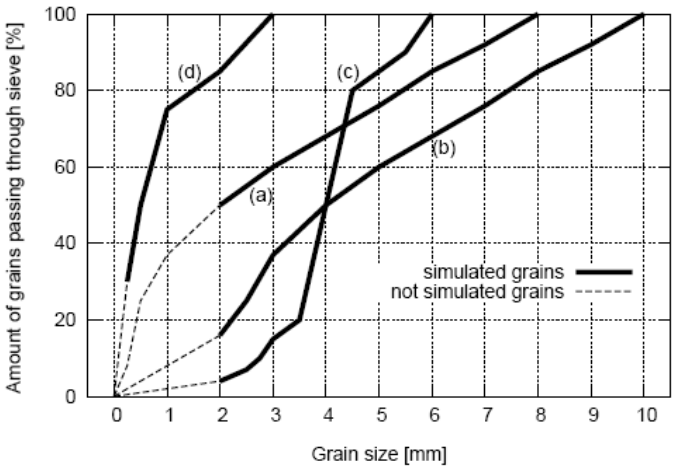

Fig. 9.25 Aggregate size distribution curves assumed for FE calculations (note that small aggregates were cut off to reduce the computation time)

The following numerical calculation program was assumed. First, three beams of a different size of sand concrete were modeled: as a partially homogeneous and partially heterogeneous with a meso-section in the notch neighborhood and as an entirely heterogeneous beam at meso-scale. The width of a heterogeneous meso-scale section b_{ms} varied between $D/2$ (40 mm) and D (80 mm) (D - beam height). These analyses allowed us to determine a representative width of a required heterogeneous region close to the notch. Next, the effect of different parameters was studied in a small-size beam. Finally, calculations were carried out with partially heterogeneous beams of a different size to determine a deterministic size effect. Three-five different stochastic realizations were usually performed for the same case. The width of the fracture process zone above the notch in all beams was determined at the deflection of u=0.15 mm on the basis of a non-local softening strain measure. As the cut-off value, $\overline{\varepsilon}_{\min}$ =0.025 was always assumed at the maximum mid-point value of $\overline{\varepsilon}_{\max}$ =0.08-0.13.

Our combined macro-mesoscopic simulations (Skarżyński and Tejchman 2010) are similar to a multi-scale approach using a Coupled Volume method where the size of a macro-element equals the size of a meso-cell (to avoid the assumption of any size of RVE) (Gitman et al. 2008). However, our simulations are faster because there is no need to continuously move between 2 calculation levels (the effect of an insignificant number of finite elements in a homogeneous beam region on the computation time is practically negligible).

First, the macro-scale calculations were carried out. Concrete was treated as an entirely homogeneous one phase-material with the following material constants: E=38500 MPa, υ=0.2, κ_0=1.3×10^{-4}, α=0.95, β=400 and l_c=2 mm. Totally, 12'000-92'000 triangular elements were assumed. The size of triangular finite elements was s=1.5 mm (in the nearest neighbourhood of the notch). Figure 9.26 presents

the FE results of the nominal strength $\sigma_n = 1.5Pl/(bD^2)$ of 3 different concrete beams versus the normalized deflection *u/D* (*P* - vertical force, *u* - beam deflection, *D* - beam height, *b* - beam width, *l=3×D* - beam span) as compared to laboratory tests by Le Belléǧo et al. (2003). Figure 9.27 shows the distribution of a non-local softening strain measure in beams.

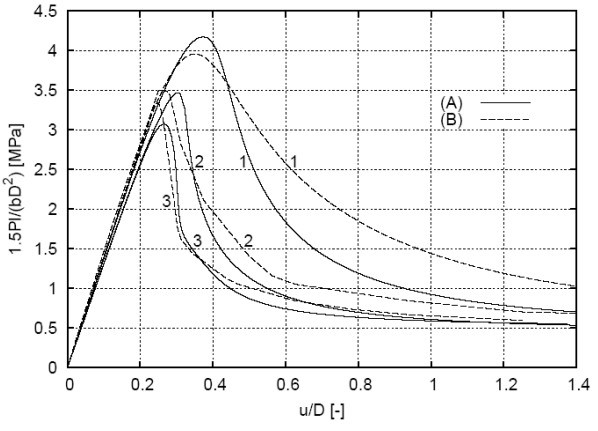

Fig. 9.26 Calculated and experimental nominal strength $1.5Pl/(bD^2)$ versus normalised beam deflection *u/D* (*u* - beam deflection, *D* - beam height): A) FE-results, B) experiments by Le Belléǧo et al. (2003), 1) small-size beam, 2) medium-size beam, 3) large-size beam (homogeneous one-phase material, l_c=2 mm) (Skarżyński and Tejchman 2010)

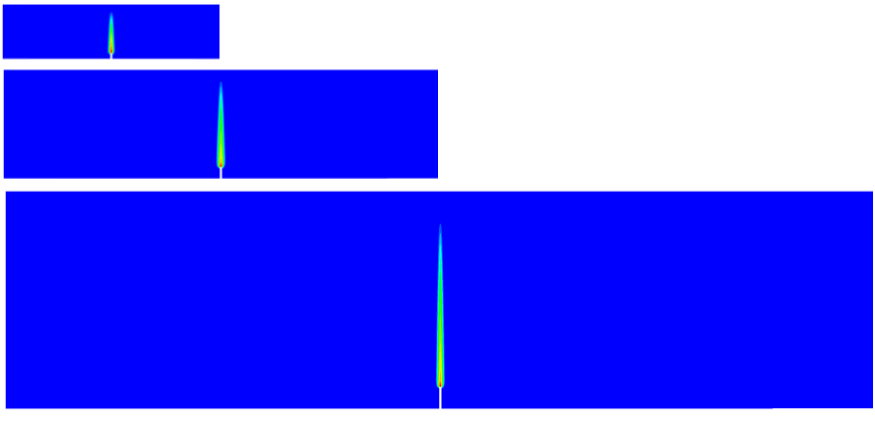

Fig. 9.27 Distribution of non-local strain measure above notch from numerical calculations with homogeneous one-phase material (at *u/D*=0.5) for small-size (top row), medium-size (medium row) and large-size beam (bottom row) (Skarżyński and Tejchman 2010)

The numerical strength results are in a satisfactory agreement with tests by Le Bellĕgo et al. (2003). The size effect is realistically described (nominal strength and material ductility increase with decreasing beam size). The width of a localized zone above the notch is about w_c=6.0 mm=3×l_c=4×s (at u/D=0.5) and approximately corresponds to the measured maximum value of w_c (5.5 mm) by DIC. However, in contrast to experiments, the calculated localized zones are always straight (an assumption of a stochastic spatially correlated distribution of tensile strength in the beam did not significantly affect their shape, Chapter 8).

Effect of width of meso-scale region

Figure 9.28 demonstrates the load-deflection curves obtained for two different aggregate distributions to determine a realistic width of a meso-scale region close to the notch (to reduce computation time). Concrete was treated in a meso-scale region as a random three-phase heterogeneous material with circularly-shaped aggregate using material constants from Tab. 9.2. In the remaining region, the material was homogeneous one-phase material (E=38500 MPa, υ=0.2, κ_0=1.3×10^{-4}, α=0.95, β=200). The beam size was 80×320 mm^2. The width of a meso-scale region was b_{ms}=40 mm or b_{ms}=80 mm (Fig. 9.29). Totally 65'000-110'000 finite elements were assumed. The characteristic length was l_c=1.5 mm and the aggregate density 30%. An entirely heterogeneous beam with 365000 elements served as the reference beam. For a comparison, a stochastic distribution of aggregate was always the same in a meso-scale section. Figure 9.30 shows the distribution of a non-local softening parameter above the notch.

The results show that the effect of the width of the meso-scale region on the results can be significant if b_{ms}≤D/2. However, if the width of a meso-scale region close to the notch equals D=80 mm, the results of forces and strains with an entirely and a partially heterogeneous beam are similar. In further calculations to save computational time, a representative meso-scale section was assumed to be always equal to the beam height b_{ms}=D (i.e. 80 mm for a small-size beam, 160 mm for a medium-size beam and 320 mm for a large-size beam).

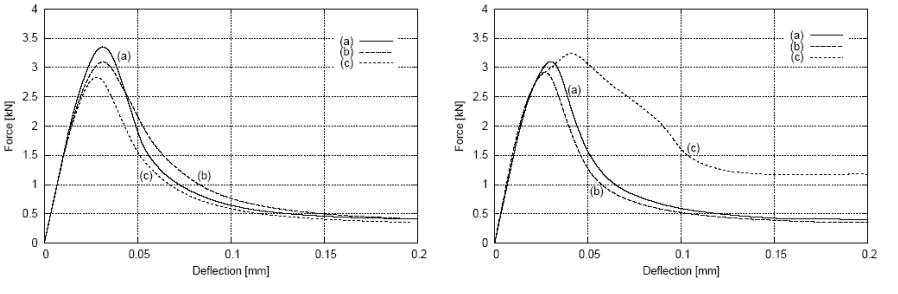

Fig. 9.28 Calculated force-deflection curves for two different random distributions of aggregate in small-size beam 80×320 mm^2 of sand concrete (d_{50}=2 mm, d_{max}=8 mm, l_c=1.5 mm): a) entirely heterogeneous beam, b) partially heterogeneous beam with width of meso-scale section of b_{ms}=80 mm, c) partially heterogeneous beam with width of the meso-scale section of b_{ms}=40 mm (Skarżyński and Tejchman 2010)

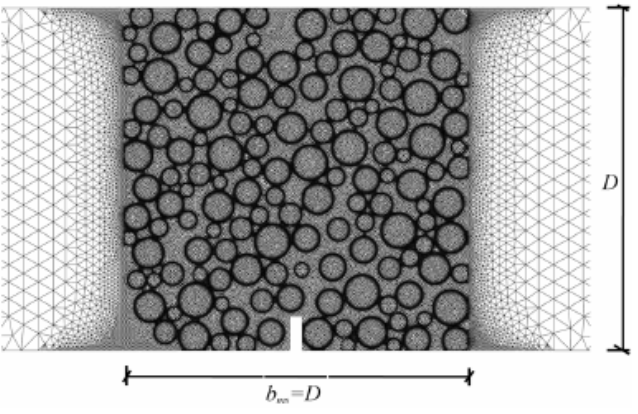

Fig. 9.29 FE mesh: three-phase heterogeneous concrete in notch neighbourhood with round shaped aggregate, cement matrix and interfacial transition zones ITZ and one-phase homogeneous concrete in remaining region (Skarżyński and Tejchman 2010)

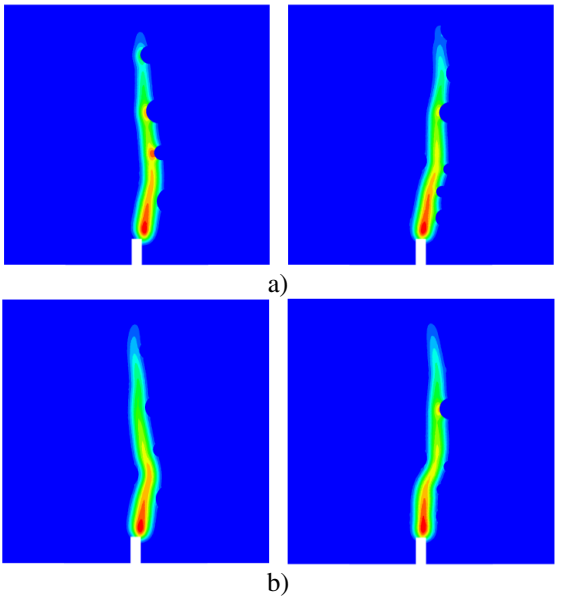

Fig. 9.30 Calculated distribution of non-local strain measure above notch (small size beam 80×320 mm^2, l_c=1.5 mm) for gravel concrete (d_{50}=2 mm, d_{max}=8 mm): a) entirely heterogeneous beam, b) partially heterogeneous beam with width of meso-scale section of b_{ms}=80 mm, c) partially heterogeneous beam with width of the meso-scale section of b_{ms}=40 mm (Skarżyński and Tejchman 2010)

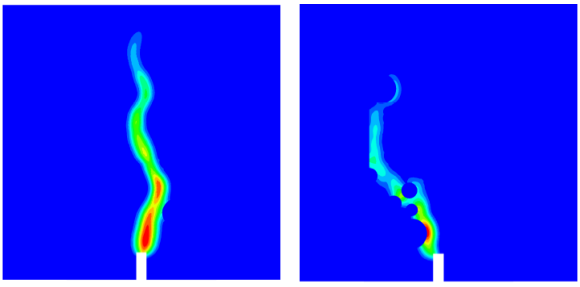

c)

Fig. 9.30 (*continued*)

Next the numerical 2D effect of different parameters such as the aggregate distribution, aggregate volume, aggregate shape, aggregate stiffness, bond thickness, notch size and characteristic length on the material behaviour (load-deflection curve and strain localization) was investigated for the small concrete beam 80×320 mm^2. The parameters were varied independently.

Effect of stochastic aggregate distribution

The effect of a random distribution of round-shaped aggregate particles in the concrete beam on the force-deflection diagram and width of a localized zone is shown in Figs. 9.31 and 9.32. The aggregate volume was ρ=45% using two aggregate size distribution curves '*a*' (d_{50}=2 mm, d_{max}=8 mm) and '*d*' (d_{50}=0.5 mm, d_{max}=3 mm) of Fig. 9.25, respectively. The ITZ thickness was t_b=0.25 mm.

All stochastic force-deflection curves are obviously the same in the almost entire elastic regime. However, they are significantly different at and after the peak (Fig. 9.31) due to a localized zone propagating between aggregate distributed at random, which is always non-symmetric and curved (Fig. 9.32). The difference in the strength is about 10-20%. The calculated width of a localized zone is approximately w_c=4.5 mm=3×l_c=9×s_{cm} independently of d_{max} and d_{50} (as in our tests, Skarżyński et al. 2011). The calculated localized zone is created at about u/D=0.0003 (u=0.024 mm) and its width increases during the deformation process.

A similar strong stochastic effect was also observed in FE calculations by Gitman et al. (2007) and He (2010). Surprisingly, a negligible stochastic effect was found in FE simulations by Kim and Abu Al-Rub (2011).

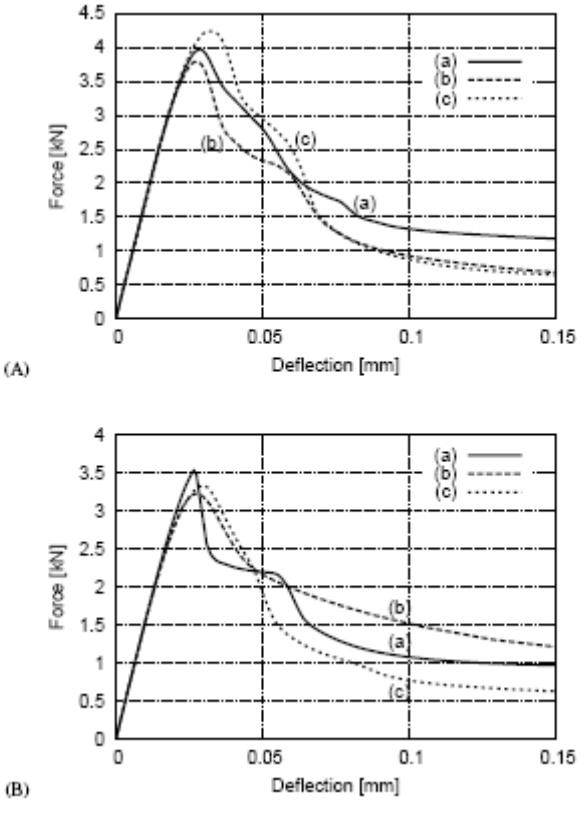

Fig. 9.3l Calculated force-deflection curves for fine-grained concrete beam (l_c=1.5 mm, ρ=45%, t_b=0.25 mm): A) with aggregate size distribution curve '*a*' of Fig. 9.25 (d_{50}=2 mm and d_{max}=8 mm) and B) with aggregate size distribution curve '*d*' of Fig. 9.25 (d_{50}=0.5 mm and d_{max}=3 mm) for three random distributions of circular aggregates (curves '*a*', '*b*' and '*c*')

Effect of aggregate shape and aggregate size distribution

To model the effect of the aggregate shape, four different grain shapes were taken into account, namely: circular, octagonal, irregular (angular) and rhomboidal (Fig. 9.33) keeping always the volume fraction and centres of grains constant (l_c=1.5 mm, ρ=60%, t_b=0.25 mm).

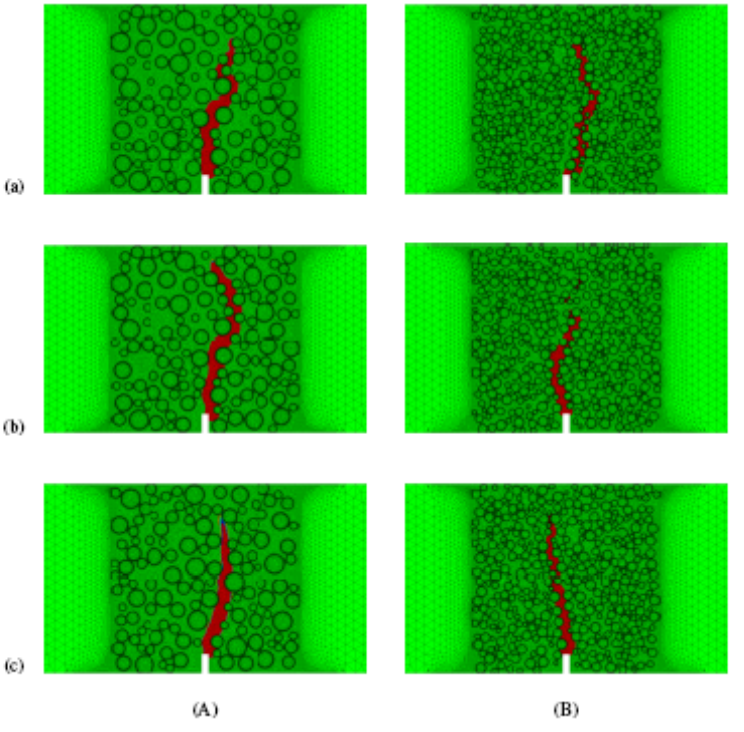

Fig. 9.32 Calculated localized zone in fine-grained concrete beam in notch region based on distribution of non-local strain measure corresponding to load-deflection curves '*a*', '*b*' and '*c*' of Figs. 9.31A and 9.31B (l_c=1.5 mm, ρ=45%, t_b=0.25 mm)

The aggregate shape can have a different influence on the beam ultimate strength depending upon the aggregate size distribution (Figs. 9.34 and 9.35). For the aggregate size distribution of Fig. 9.25a, the ultimate beam strength is the highest for rhomboidal-shaped particles and the lowest for octagonal-shaped particles (Figs. 9.33a, 9.35B and 9.35D). This difference equals even 30%. In the case of the aggregate size distribution curve of Fig. 9.25b, the ultimate beam strength is similar for all assumed particle shapes (Fig. 9.34B). For the aggregate size distribution of Fig. 9.25c, angular-shaped inclusions have the lower tensile strength than circular grains (Fig. 9.35C). From simulations follows that the mean tensile strength is usually higher with the larger mean grain size and the narrower grain range (Figs. 9.34A, 9.34B, 9.34C and 9.35).

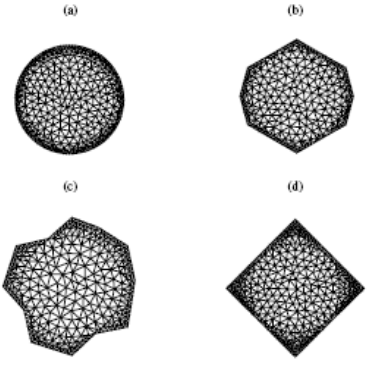

Fig. 9.33 Aggregate shape assumed in calculations: a) circular, b) octagonal, c) irregular (angular), d) rhomboidal

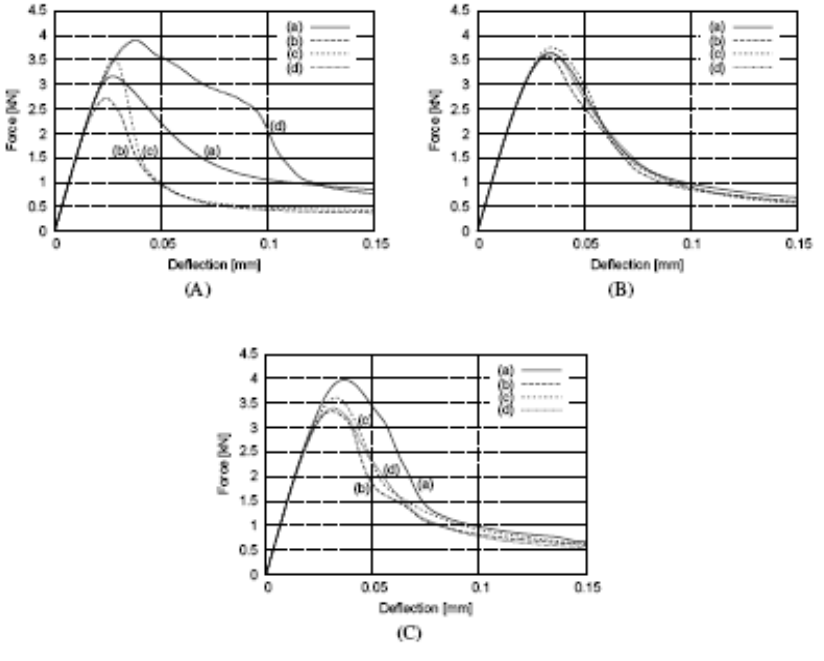

Fig. 9.34 Calculated force-deflection curves for different aggregate shape of Fig. 9.33: a) circular, b) octagonal, c) irregular (angular), d) rhomboidal (fine-grained concrete beam 80×320 mm^2, l_c=1.5 mm, ρ=60%, t_b=0.25 mm) and different aggregate size distributions of Fig. 9.25: A) d_{50}=2 mm and d_{max}=8 mm (curve '*a*'), B) d_{50}=4 mm and d_{max}=10 mm (curve '*b*'), C) d_{50}=4 mm and d_{max}=6 mm (curve '*c*')

The width of a localized zone equals approximately w_c=3 mm for ρ=60% and is not influenced by the aggregate shape, aggregate distribution, mean and maximum grain size (Fig. 9.36). In turn, the form of a localized zone is strongly affected by the aggregate shape contributing thus to the different strength. The calculated width of a localized zone is in good agreement with our experiments with fine-grained concrete (Figs. 9.23 and 9.24A). Our outcome is in contrast to statements by Bažant and Pijauder-Cabot (1989), and Bažant and Oh (1983) wherein the width of a localized zone in usual concrete was estimated to be dependent upon d_{max}. It is also in contrast to experimental results by Mihashi and Nomura (1996) which showed that the width of a localized zone in usual concrete increased with increasing aggregate size. The differences between our and the experimental results (Bažant and Oh 1983, Mihashi and Nomura 1996) lie probably in a different concrete mix, specimen size and loading type. For instance, in our other tests with large reinforced concrete beams 6.0 m long without shear reinforcement under bending, the width of a localized zone in usual concrete was about 15 mm indicating that l_c=5 mm (Syroka and Tejchman 2011). This problem merits further experimental and numerical investigations.

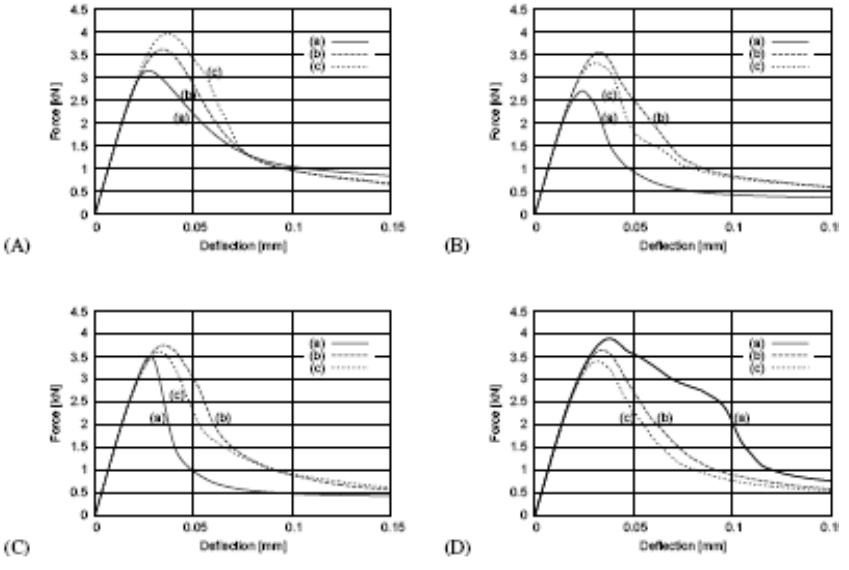

Fig. 9.35 Calculated force-deflection curves for different aggregate shape of Fig. 9.33: A) circular, B) octagonal, C) irregular (angular), D) rhomboidal (fine-grained concrete beam 80×320 mm^2, l_c=1.5 mm, ρ=60%, t_b=0.25 mm) and different aggregate size distribution of Fig. 9.25: a) d_{50}=2 mm and d_{max}=8 mm (curve '*a*'), b) d_{50}=4 mm and d_{max}=10 mm (curve '*b*'), c) d_{50}=4 mm and d_{max}=6 mm (curve '*c*')

According to Kim and Abu Al-Rub (2011) the aggregate shape has a weak effect on the ultimate strength of concrete and on the strain to damage-onset, but significantly affects the crack initiation, propagation and distribution. The stress concentrations at sharp edges of polygonal particles cause that the ultimate tensile strength and strain at the damage onset are the highest for circular grains model. Similar conclusions were derived by He et al. (2009) and He (2010).

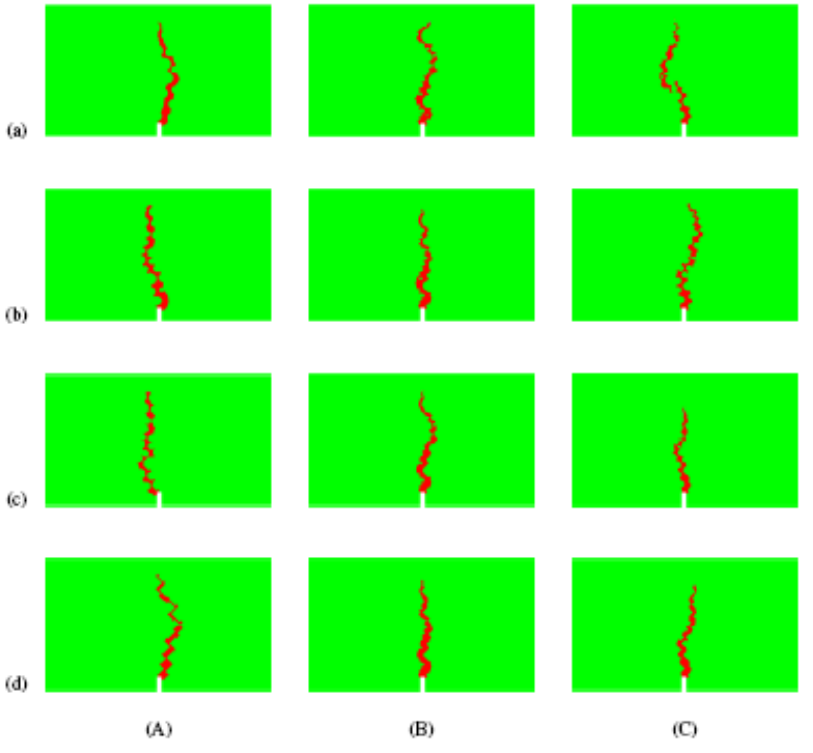

Fig. 9.36 Calculated localized zone based on distribution of non-local strain measure in fine-grained concrete beam in notch region corresponding to load-deflection curves '*a*', '*b*', '*c*' and '*d*' of Figs. 9.34A, 9.34B and 9.34C (l_c=1.5 mm, ρ=60%, t_b=0.25 mm)

Effect of volume fraction of aggregate

Circular grains with the volume of ρ=30%, ρ=45% and ρ=60% were used (l_c=1.5 mm, t_b=0.25 mm), Fig. 9.37. Figures 9.38 and 9.39 demonstrate the effect of the aggregate volume in fine-grained concrete beam with the aggregate size distributions '*a*' of Fig. 9.25 (d_{50}=2 mm, d_{max}=8 mm) and '*d*' of Fig. 9.25 (d_{50}=0.5 mm, d_{max}=3 mm).

In our FE simulations, the Young modulus and ultimate beam strength increase with increasing aggregate density in the range of 30%-60% (Fig. 9.38). This increase certainly depends on material parameters assumed for separated concrete phases, in particular for ITZs being always the weakest parts in concrete.

The width and shape of a localized zone are influenced by the aggregate volume; a localized zone becomes narrower with increasing aggregate volume: w_c=6 mm at ρ=30%, w_c=4.5 mm at ρ=45% and w_c=3 mm at ρ=60% (Fig. 9.39).

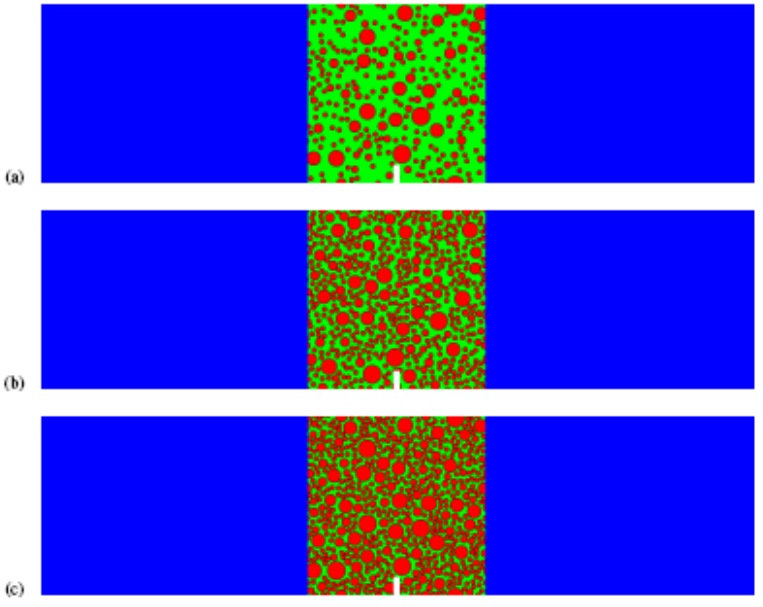

Fig. 9.37 Concrete beams with different volume fraction of aggregate ρ in region close to notch: a) ρ=30%, b) ρ=45% and c) ρ=60% using grain size distribution '*a*' of Fig. 9.25

According to Kim and Abu Al-Rub (2011) the Young modulus linearly increases with increasing aggregate volume, and the tensile strength decreases with increasing aggregate density up to ρ=40% and increases next from ρ=40% up to ρ=60%. The strain at the damage linearly decreases with increasing aggregate volume. He et al. (2009) and He (2010) concluded that concrete with a higher packing density of aggregate up to 50% has a decreasing tensile strength (due to a higher number of very weak interfacial transitional zones around aggregate). It seems that the property of ITZ (stiffness, strength and width) is essential for the global strength versus ρ.

Effect of ITZ thickness

The interfacial transition zone (ITZ) is a special region of the cement paste around particles, which is perturbed by their presence. Its origin lies in the packing of the cement grains against the much larger aggregate which leads to a local increase in porosity (micro-voids) and a presence of smaller cement particles. A paste with lower *w/c* (higher packing density) or made with finer cement particles leads to

ITZ of smaller extent. This layer is highly heterogeneous and damaged and thus critical for the concrete behaviour (Srivener et al. 2004, Mondal et al. 2009). An accurate understanding of the properties and behaviour of ITZ is one of the most important issues in the meso-scale analysis because damage is initiated at the weakest region and ITZ is just this weakest link in concrete. We assumed that ITZs have the reduced stiffness and strength as compared to the cement matrix (Tabl.9.2).

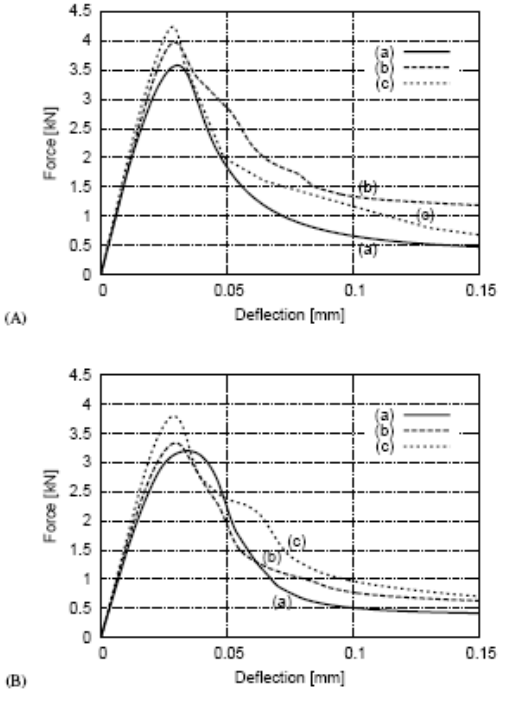

Fig. 9.38 Calculated load-deflection curves for different volume fractions ρ of circular aggregate: a) ρ=30%, b) ρ=45% and c) ρ=60% (concrete beam 80×320 mm^2, l_c=1.5 mm, t_b=0.25 mm, A) aggregate size distribution '*a*' of Fig. 9.25 (d_{50}=2 mm, d_{max}=8 mm), B) aggregate size distribution '*d*' of Fig. 9.25 (d_{50}=0.5 mm, d_{max}=3 mm)

Figures 9.40 and 9.41 demonstrate the effect of the ITZ thickness in a fine-grained concrete beam of circular grains with the aggregate size distribution '*a*' of Fig. 9.25 (d_{50}=2 mm, d_{max}=8 mm) assuming the aggregate volume fraction ρ=45% and ρ=60% (l_c=1.5 mm). Since there is very limited data on the thickness of ITZ, the thickness t_b in our study was assumed to be 0 mm, 0.05mm (He et al. 2011, He 2010), 0.25 mm (Gitman et al. 2007) and 0.75 mm.

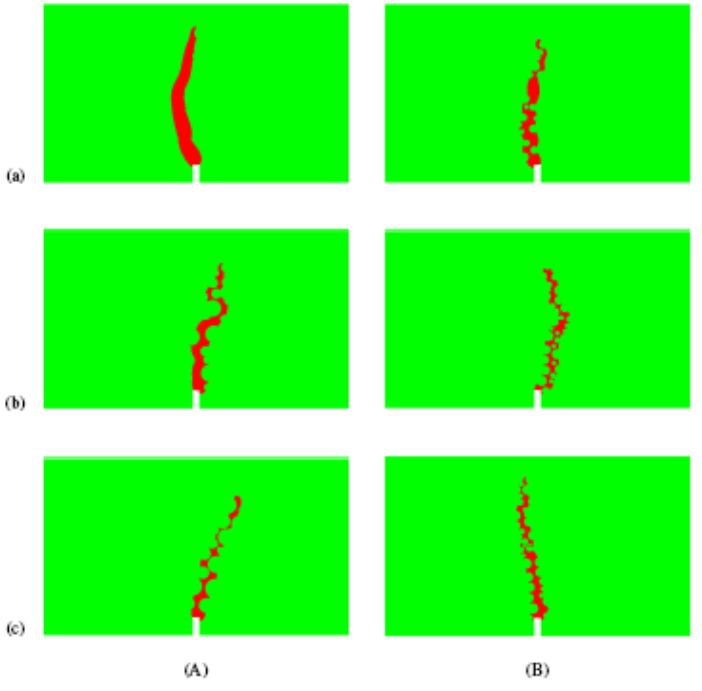

Fig. 9.39 Calculated localized zone based on distribution of non-local strain measure in fine-grained concrete beam 80×320 mm^2 (l_c=1.5 mm, t_b=0.25 mm) corresponding to load-deflection curves '*a*', '*b*' and '*c*' of Figs. 9.38A and 9.38B

The results show that the thickness and strength of ITZs strongly affect both the load-displacement response and shape of localized zone. Since ITZ is the weakest phase, the ultimate beam strength decreases with increasing bond thickness (Fig. 9.40). This result is in agreement with those by He et al. (2009), He (2010) and Kim and Abu Al-Rub (2011). However, the residual strength rather increases with increasing bond thickness as in calculations by Kim and Abu Al-Rub (2011). The width of a localized zone is w_c=4.5 mm (ρ=45%) and w_c=3 mm (ρ=60%) and is not affected by the ITZ size t_b (Fig. 9.41).

Effect of notch size

Figures 9.42 and 9.43 demonstrate the effect of the notch size on the load-deflection diagram and strain localization in a fine-grained concrete beam with a random distribution of aggregate '*a*' of Fig. 9.25 (d_{50}=2 mm to d_{max}=8 mm) using circular aggregate volume ρ=30% and ρ=60% (l_c=1.5 mm, t_b=0.25 mm). The notch size was 0×0 mm^2, 3×3 mm^2 and 6×3 mm^2 (width×height), respectively. The beam without notch was modelled as entirely heterogeneous to be sure that a localized zone occurs in a meso-region.

The ultimate beam strength is higher with decreasing notch size (Fig. 9.42). The notch size has no influence on the width of a localized zone (w_c=6 mm at ρ=30% and w_c=3 mm at ρ=60% (Fig. 9.43).

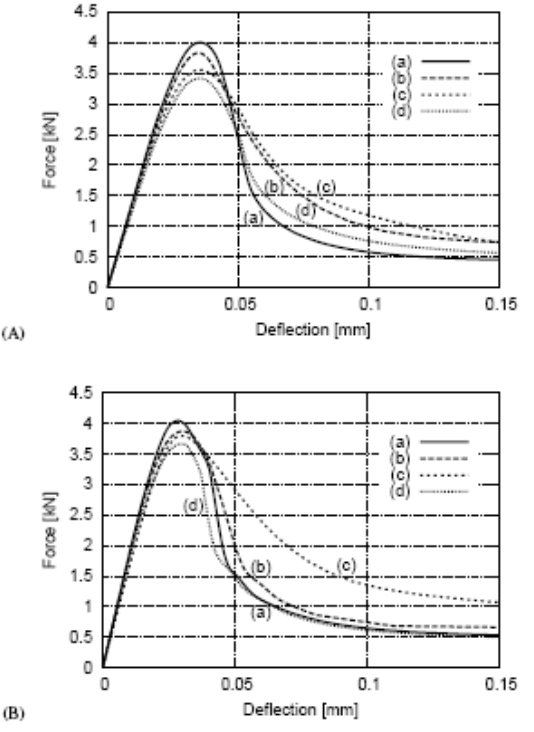

Fig. 9.40 Numerical effect of different ITZ thickness t_b in FE calculations on load-deflection curve: a) t_b=0 mm, b) t_b=0.05 mm, c) t_b=0.25 mm and d) t_b=0.75 mm, A) ρ=45%, B) ρ=60% (fine-grained concrete beam 80×320 mm^2, l_c=1.5 mm, circular grains with size distribution '*a*' of Fig. 9.25 (d_{50}=2 mm, d_{max}=8 mm)

Effect of aggregate stiffness

Figure 9.44 shows the effect of the aggregate stiffness in a small size beam (80×320 mm^2, d_{50}=4 mm and d_{max}=10 mm, ρ=60%, t_b=0.25 mm, l_c=1.5 mm). The calculations were carried out with weak aggregate (which had the same properties as ITZ of Tab. 9.2).

For the weak aggregate, a localized zone can propagate through weak grains. The vertical force is obviously smaller and the width of a localized zone is higher as compared to the results with the strong aggregate (strong aggregate - w_c=3.3 mm, weak aggregate - w_c=5.8 mm).

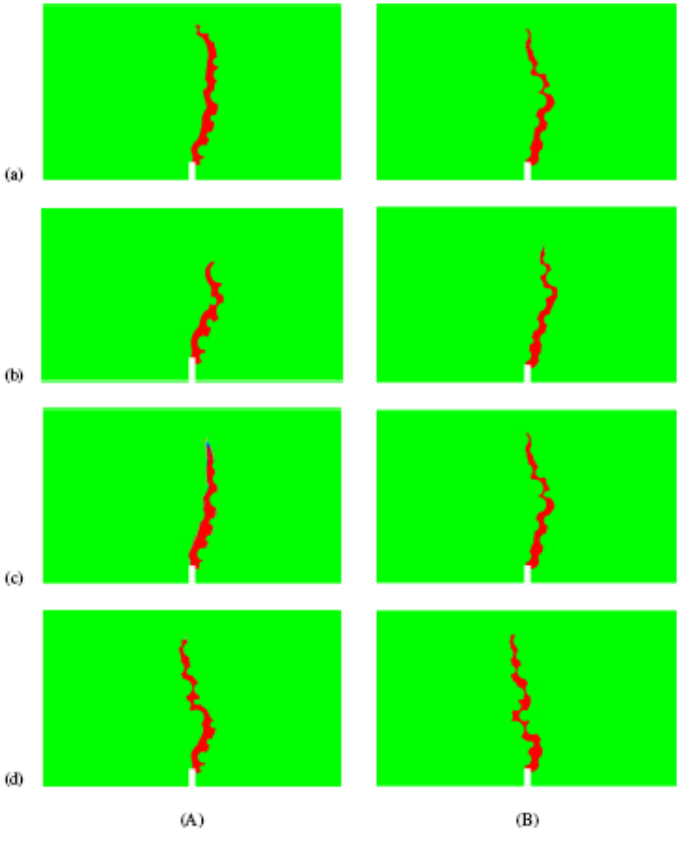

Fig. 9.41 Numerical effect of different bond thickness t_b in FE calculations on distribution of non-local strain measure close to beam notch corresponding to load-deflection curves '*a*', '*b*', '*c*' and '*d*' of Figs. 9.40A and 9.40B

Effect of characteristic length of micro-structure

The effect of a characteristic length of micro-structure on the load-deflection diagram and strain localization is shown in Figs. 9.45 and 9.46 using the same stochastic distribution of circular aggregate (l_c changed between 0.5 mm and 5 mm).

With increasing characteristic length, both beam strength and width of a localized zone strongly increase since the material softening decreases and material becomes more ductile. A pronounced deterministic size effect occurs. A localized zone propagating in a cement matrix between aggregate grains is strongly curved at l_c=0.5-2.5 mm, whereas it becomes more straight at l_c>2.5 mm.

It is about: w_c=2.9-17.6 mm=(3.5-5.9)×l_c=(5.8-35.2)×d_{50} at ρ=30%, w_c=2.5-16.7 mm=(3.0-5.0)×l_c=(1.25-8.35)×d_{50} at ρ=45% and w_c=2.4-13.9 mm=(2.3-4.7)×l_c=(0.6-3.47)×d_{50} at ρ=60% (Tab. 9.3). It always decreases with increasing ρ (Tab. 9.3). A characteristic length of micro-structure is not uniquely connected to the aggregate size.

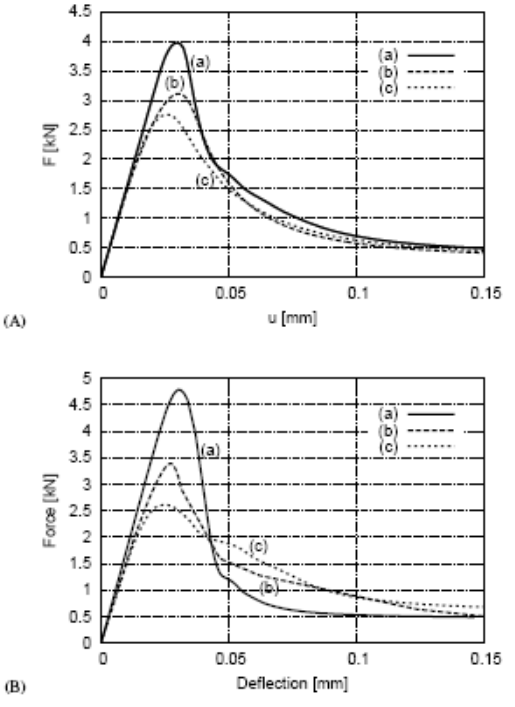

Fig. 9.42 Numerical effect of notch size on force-deflection curve for two different aggregate densities: a) 0×0 mm^2, b) 3×3 mm^2 and c) 6×3 mm^2, A) ρ=30%, B) ρ=60% (fine-grained concrete beam 80×320 mm^2, l_c=1.5 mm, circular aggregate distribution '*a*' of Fig. 9.25 with d_{50}=2 mm and d_{max}=8 mm)

Figure 9.47 shows the evolution of the width and height of the localized zone from FE calculations. The FE results of Fig. 9.47 are similar as in the experiments (Fig. 9.25). The calculated maximum width is 3.25 mm (3.5-4.0 mm in tests) and height 55 mm (50-55 mm in tests) at u=0.2 mm. The calculated localized zone strongly forms (linearly) before and after the maximum vertical force in the range of u=0.025-0.05 mm (width) and of u=0.025-0.1 mm (length). The mean propagation rate of the calculated localized zone versus the beam deflection is similar as in experiments, although is more uniform (Fig. 9.48). In the experiments, a macro-crack occurred at about u=0.04 mm, which cannot be captured by our model. In order to numerically describe a macro-crack, a discontinuous approach has to be used (e.g. XFEM or cohesive crack model, Chapter 4).

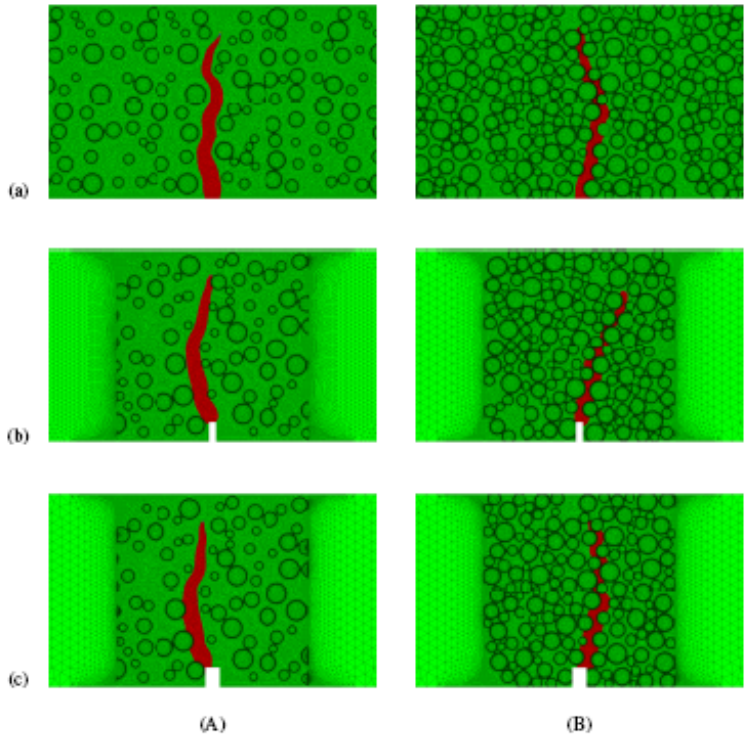

Fig. 9.43 Numerical effect of notch size on distribution of non-local strain measure close to beam notch corresponding to load-deflection curves '*a*', '*b*' and '*c*' of Figs. 9.42A and 9.42B

Effect of beam size

The effect of the beam size is presented in Figs. 9.49 and 9.50. Figure 9.49 shows the numerical results of the nominal strength $\sigma_n = 1.5Pl/(bD^2)$ versus the normalized deflection *u/D* for three different concrete beams compared to tests by Le Bellĕgo et al. (2003). Concrete was treated as an one-phase material with a heterogeneous three-phase section close to the notch (b_{ms}=D) using material constants from Tab. 9.2. The following amount of triangular finite elements was used: 110'000 (small beam), 420'000 medium beam and 1'600'000 (large beam). In turn, Figure 9.50 presents the distribution of a non-local softening strain measure in beams. The calculations were carried out with gravel concrete of d_{max}=8 mm, aggregate density of ρ=30% and a characteristic length of l_c=1.5 mm.

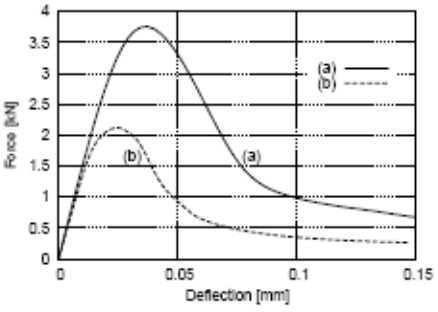

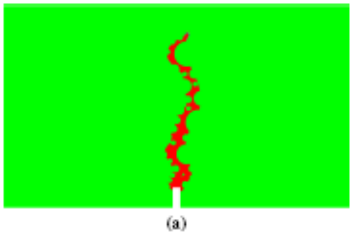

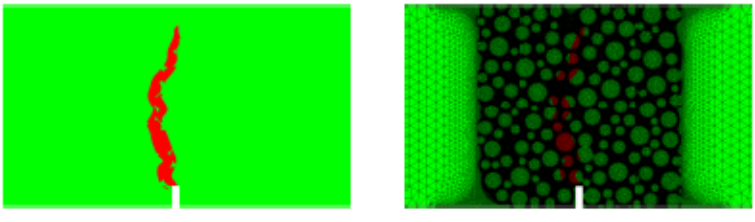

Fig. 9.44 Effect of aggregate stiffness on force-deflection curve and distribution of non-local strain measure close to beam notch: a) strong circular aggregate, b) weak circular aggregate (fine-grained concrete beam 80×320 mm^2, l_c=1.5 mm, circular aggregate distribution '*c*' of Fig. 9.25 with d_{50}=4 mm and d_{max}=10 mm, ρ=60%)

The numerical results are in a satisfactory agreement with tests by Le Bellĕgo et al. (2003). The deterministic size effect is realistically modelled in calculations. The width of the localized zone above the notch at *u/D*=0.5 is 6 mm (ρ=30%) for all beam sizes. The localized zone propagating between aggregate is always strongly curved, what satisfactorily reflects the experimental results.

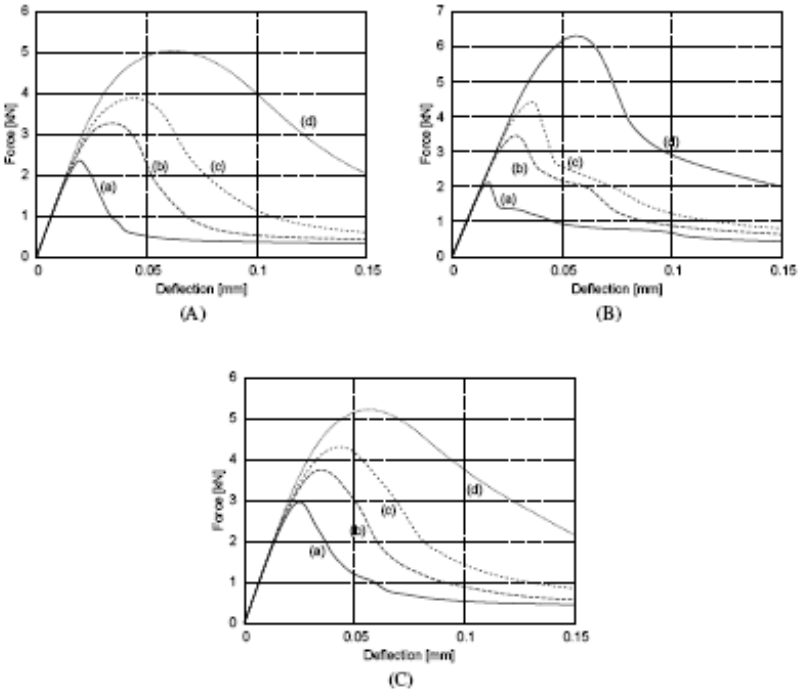

Fig. 9.45 Calculated load-deflection curves for different characteristic lengths l_c: a) l_c=0.5 mm, b) l_c=1.5 mm, c) l_c=2.5 mm and d) l_c=5 mm (concrete beam 80×320 mm^2, ITZ thickness t_b=0.25 mm), A) volume fraction of circular aggregate ρ=30% (concrete mix '*d*' of Fig. 9.25 with d_{50}=0.5 mm and d_{max}=3 mm), B) volume fraction of circular aggregate ρ=45% (concrete mix '*a*' of Fig. 9.25 with d_{50}=2 mm and d_{max}=8 mm), C) volume fraction of angular aggregate ρ=60% (concrete mix '*b*' of Fig. 9.25 with d_{50}=4 mm and d_{max}=10 mm)

Figure 9.51 shows a comparison between the measured and calculated size effect for concrete beams. In addition, the results of a deterministic size effect law by Bažant, Eq. 5.5 (Bažant and Planas 1998, Bažant 2004) are enclosed (which is valid for structures with pre-existing notches, Chapter 8). The experimental and theoretical beam strength shows a strong parabolic size dependence. The experimental and numerical results match quite well the size effect law by Bažant (Bažant and Planas 1998).

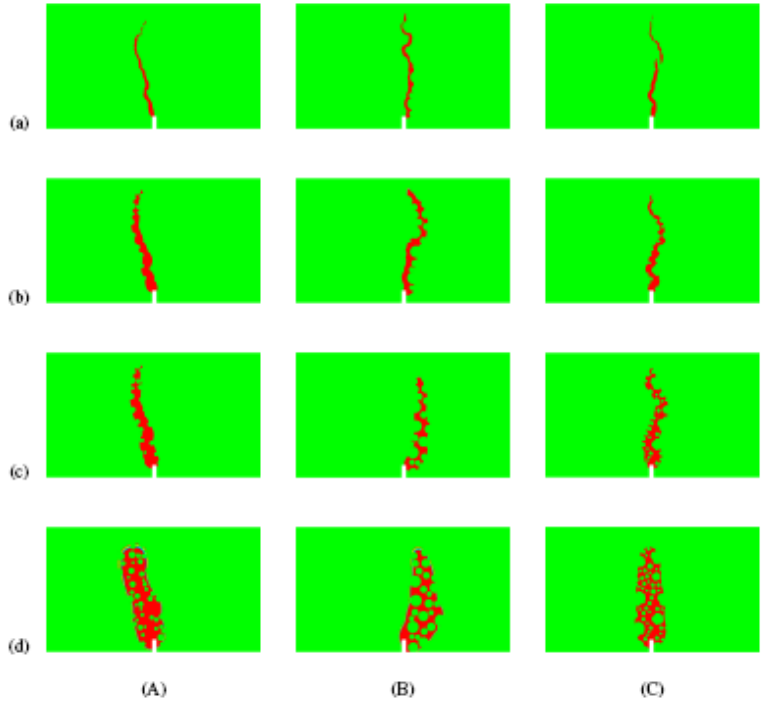

Fig. 9.46 Calculated localized zone based on distribution of non-local strain measure for different characteristic lengths l_c: a) l_c=0.5 mm, b) l_c=1.5 mm, c) l_c=2.5 mm and d) l_c=5 mm (concrete beam 80×320 mm^2, bond thickness t_b=0.25 mm), A) volume fraction of circular aggregate ρ=30% (concrete mix '*d*' of Fig. 9.25 with d_{50}=0.5 mm and d_{max}=3 mm), B) volume fraction of circular aggregate ρ=45% (concrete mix '*a*' of Fig. 9.25 with d_{50}=2 mm and d_{max}=8 mm), C) volume fraction of angular aggregate ρ=60% (concrete mix '*b*' of Fig. 9.25 with d_{50}=4 mm and d_{max}=10 mm)

Table 9.3 Calculated width of localized zone with different characteristic length l_c and volume fraction ρ

Characteristic length l_c	Width of localized zone w_c [mm] for different volume fraction of aggregate ρ					
	ρ = 30%		ρ = 45%		ρ = 60%	
0.5 mm	2.9	5.9 × l_c	2.4	5.0 × l_c	2.4	4.7 × l_c
1.5 mm	6.2	4.1 × l_c	4.5	3.0 × l_c	3.5	2.3 × l_c
2.5 mm	9.3	3.7 × l_c	8.7	3.5 × l_c	6.9	2.7 × l_c
5 mm	17.6	3.5 × l_c	16.7	3.4 × l_c	13.9	2.8 × l_c

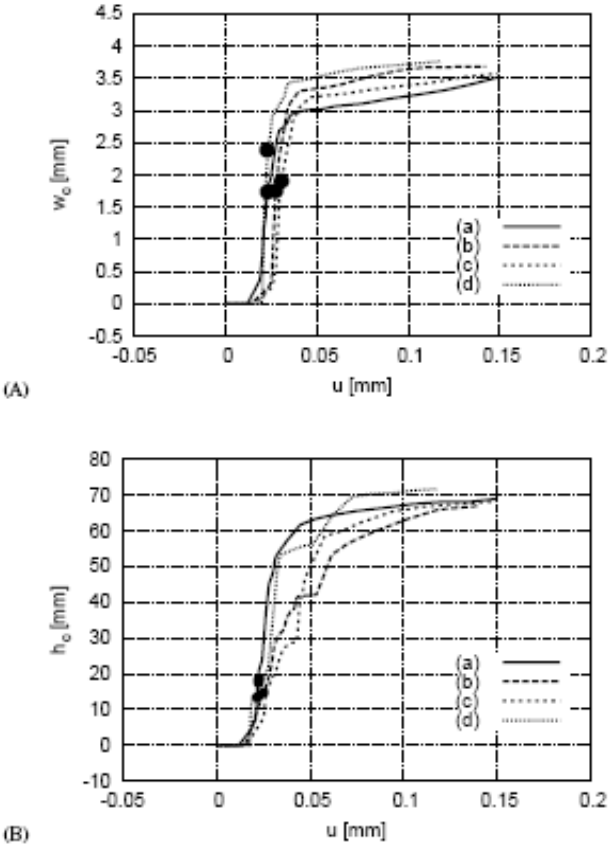

Fig. 9.47 The calculated evolution of width (A) w_c and height h_c (B) of localized zone versus beam deflection u: a) concrete mix '*a*' of Fig. 9.25 with d_{50}=2 mm and d_{max}=8 mm, irregular aggregate, ρ=60%, l_c=1.5 mm, b) concrete mix '*b*' of Fig. 9.25 with d_{50}=4 mm and d_{max}=10 mm, octagonal aggregate, ρ=60%, l_c=1.5 mm, c) concrete mix '*c*' of Fig. 9.25 with d_{50}=4 mm and d_{max}=6 mm, circular aggregate, ρ=60%, l_c=1.5 mm, d) concrete mix '*a*' of Fig. 9.25 with d_{50}=2 mm and d_{max}=8 mm, circular aggregate, ρ=60%, beam without notch, l_c=1.5 mm (• - maximum vertical force)

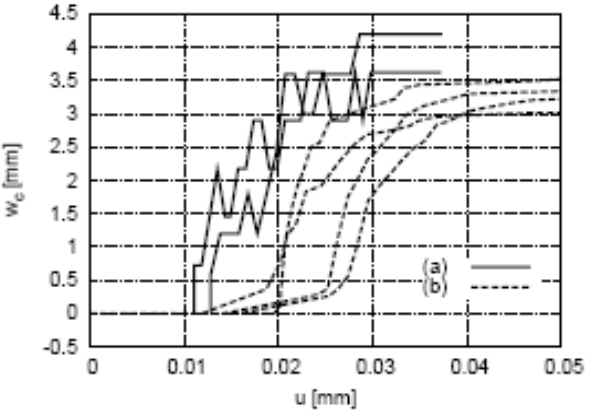

Fig. 9.48 Comparison between measured (a) and calculated (b) evolution of width of localized zone w_c versus beam deflection u (maximum vertical force occurs at deflection u=0.035 mm)

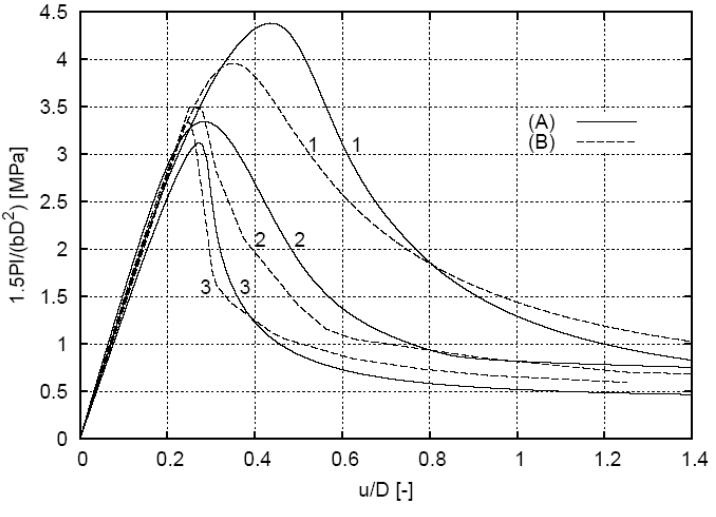

Fig. 9.49 Calculated nominal strength $1.5Pl/(bD^2)$ versus normalised beam deflection u/D (u - beam deflection, D - beam height): A) FE-results, B) experiments by Le Bellĕgo et al. (2003): 1) small-size beam, (2) medium-size beam, (3) large-size beam (three-phase random heterogeneous material close to notch, $b_{ms}=D$) (Skarżyński and Tejchman 2010)

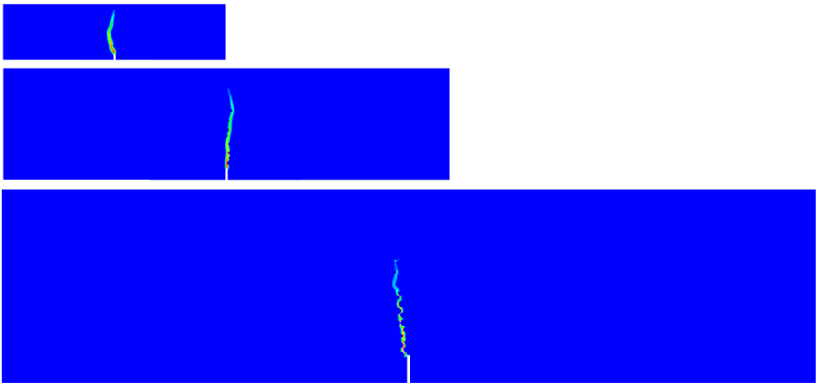

Fig. 9.50 Calculated distribution of non-local strain measure above notch from numerical calculations (at u/D=0.5) in small-size, medium-size and large-size beam (random heterogeneous three-phase material close to notch, $b_{ms}=D$) (Skarżyński and Tejchman 2010)

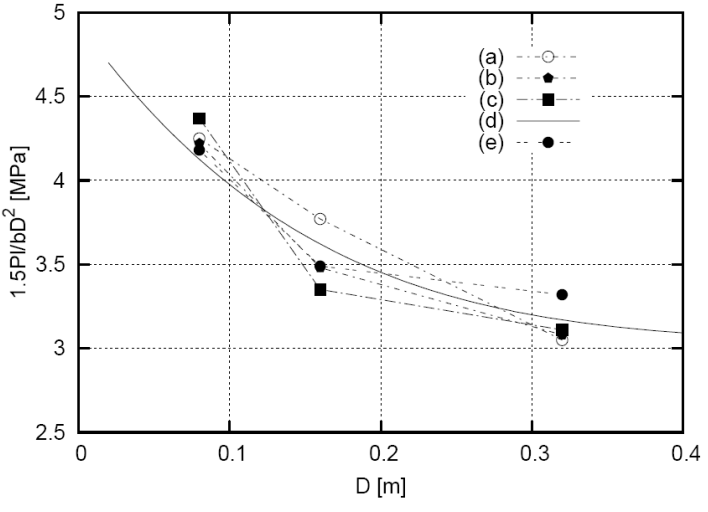

Fig. 9.51 Calculated and measured size effect in nominal strength $1.5Pl/(bD^2)$ versus beam height D for concrete beams of a similar geometry (small-, medium- and large-size beam): a) our laboratory experiments, b) our FE-calculations (homogeneous one-phase material), c) our FE-calculations (heterogeneous material close to notch, $b_{ms}=D$), d) size effect law by Bažant (2004), Eq. 5.5, e) experiments by Le Bellĕgo et al. (2003) (Skarżyński and Tejchman 2010)

9.3 Representative Volume Element

Thus, the most important issue in multi-scale analyses is determination of an appropriate size for a micro-structural model, so-called representative volume element RVE. The size of RVE should be chosen such that homogenized properties become independent of micro-structural variations and a micro-structural domain is small enough such that separation of scales is guaranteed. Many researchers attempted to define the size of RVE in heterogeneous materials with a softening response in a post-peak regime (Hill 1963, Bažant and Pijauder-Cabot 1989, Drugan and Willis 1996, Evesque 2000, van Mier 2000, Bažant and Novak 2003, Kanit et al. 2003, Kouznetsova et al. 2004, Gitman et al. 2007, Skarżyński and Tejchman 2009). The last outcomes in this topic show, however, that RVE cannot be defined in softening quasi-brittle materials due to strain localization since the material loses then its statistical homogeneity, Chapter 9.1 (Gitman et al. 2007, Skarżyński and Tejchman 2009, 2010). Thus, each multi-scale approach always suffers from non-objectivity of results with respect to a cell size. RVE solely exists for linear and hardening regimes.

The intention of our FE investigations is to determine RVE in concrete under tension using two alternative strategies (one of them was proposed by Nguyen et al. 2010) (Skarżyński and Tejchman al. 2012). Concrete was assumed at meso-scale as a random heterogeneous material composed of three phases. The FE calculations of strain localization were carried out again with a scalar isotropic damage with non-local softening (Tab. 9.4). The interface was assumed to be the weakest component (Lilliu and van Mier 2003) and its width was 0.25 mm (Gitman et al. 2007). For the sake of simplicity, the aggregate was assumed in the form of circles. The number of triangular finite elements changed between 4'000 (the smallest specimen) and 100'000 (the largest specimen). The size of triangular elements was: s_a=0.5 mm (aggregate), s_{cm}=0.25 mm (cement matrix) and s_{itz}=0.1 mm (interface). To analyze the existence of RVE under tension, a plane strain uniaxial tension test was performed with a quadratic concrete specimen representing a unit cell with the periodicity of boundary conditions and material periodicity (Chapter 9.1), Fig. 9.52.

The unit cells of six different sizes were investigated $b \times h$: 5×5 mm^2, 10×10 mm^2, 15×15 mm^2, 20×20 mm^2, 25×25 mm^2 and 30×30 mm^2, respectively. For each specimen, three different stochastic realizations were performed with the aggregate density of ρ=30% (the results for ρ=45% and ρ=60% showed the same trend). A characteristic length of micro-structure was assumed to be l_c=1.5 mm based on DIC and numerical studies with an isotropic damage model (Chapter 9.2). Thus, the maximum finite element size in 3 different concrete phases was not greater than $3 \times l_c$ to obtain mesh-objective results (Bobiński and Tejchman 2004, Marzec et al. 2007).

Table 9.4 Material properties assumed for FE calculations of 2D random heterogeneous three-phase concrete material (Skarżyński and Tejchman 2012)

Parameters	Aggregate	Cement matrix	ITZ
Modulus of elasticity E [GPa]	30	25	20
Poisson's ratio υ [-]	0.2	0.2	0.2
Crack initiation strain κ_0 [-]	0.5	8×10^{-5}	5×10^{-5}
Residual stress level α [-]	0.95	0.95	0.95
Slope of softening β [-]	200	200	200

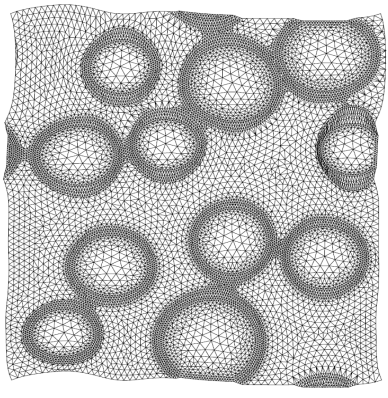

Fig. 9.52 Deformed three-phase concrete specimen with periodicity of boundary conditions and material periodicity (Skarżyński and Tejchman 2012)

Standard averaging approach

The standard averaging is performed in the entire specimen domain (Chapter 9.1). The homogenized stress and strain are defined in two dimensions as

$$<\sigma>=\frac{f_y^{\text{int}}}{b} \qquad \text{and} \qquad <\varepsilon>=\frac{u}{h}, \tag{9.4}$$

where f_y^{int} denotes the sum of all vertical nodal forces in the 'y' direction along the top edge of the specimen (Fig. 9.5), u is the prescribed vertical displacement in the 'y' direction and b and h are the width and height of the specimen.

Figure 9.53 presents the stress-strain relationships for various cell sizes and two random aggregate distributions with the material constants of Tab. 9.5 (l_c= 1.5 mm). In the first case, the aggregate distribution was similar and in the second

case it was at random in different unit cells. The results show that the stress-strain curves are the same solely in an elastic regime independently of the specimen size, aggregate density and aggregate distribution. However, they are completely different at the peak and in a softening regime. An increase of the specimen size causes a strength decrease and an increase of material brittleness (softening rate). The differences in the evolution of stress-strain curves in a softening regime are caused by strain localization (in the form of a curved localized zone propagating between aggregates, Figs. 9.54 and 9.55) contributing to a loss of material homogeneity (due to the fact that strain localization is not scaled with increasing specimen size). The width of a calculated localized zone is approximately w_c=3 mm=2×l_c=12×s_{cm} (unit cell 5×5 mm^2), w_c=5 mm=3.33×l_c=20×s_{cm} (unit cell 10×10 mm^2) and w_c=6 mm=4×l_c=24×s_{cm} (unit cells larger than 10×10 mm^2).

Figure 9.56 presents the expectation value and standard deviation of the tensile fracture energy G_f versus the specimen height h for 3 different realizations. The fracture energy G_f was calculated as the area under the strain-stress curves g_f multiplied by the width of a localized zone w_c

$$G_f = g_f \times w_c = (\int_{a_1}^{a_2} <\sigma> \mathrm{d} <\varepsilon>) \times w_c \,. \tag{9.4}$$

The integration limits 'a_1' and 'a_2' are 0 and 0.001, respectively. The fracture energy decreases with increasing specimen size without reaching an asymptote, i.e. the size dependence of RVE exists (since a localized zone does not scale with the specimen size). Thus, RVE cannot be found for softening materials and a standard averaging approach cannot be used in homogenization-based multi-scale models.

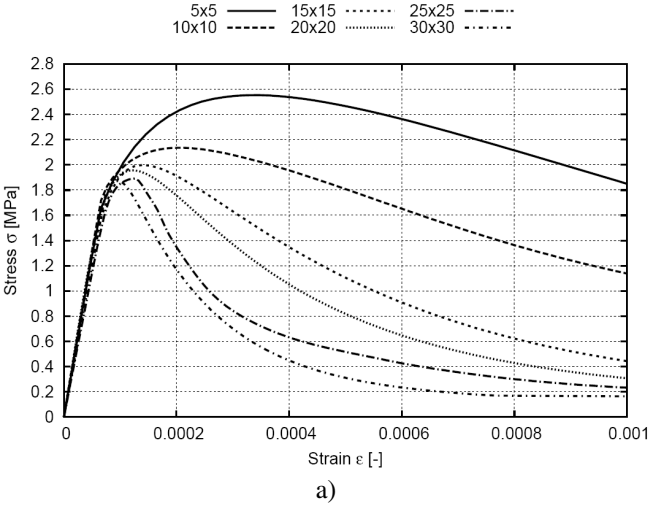

a)

Fig. 9.53 Stress-strain curves for various sizes of concrete specimens and two different random distributions of aggregate (a) and (b) using standard averaging procedure (characteristic length l_c=1.5 mm, aggregate density ρ=30%) (Skarżyński and Tejchman 2012)

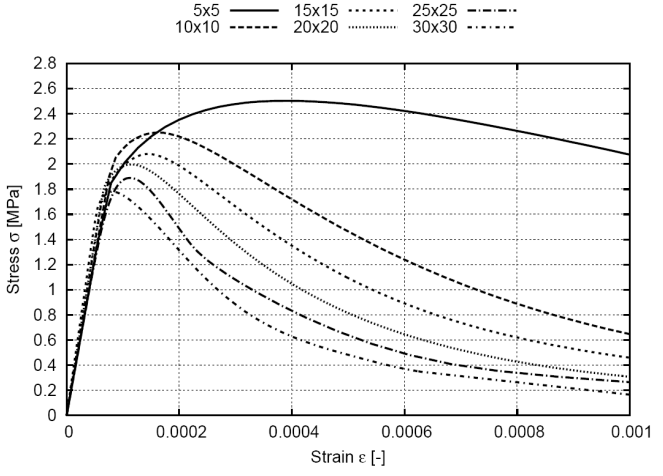

b)

Fig. 9.53 (*continued*)

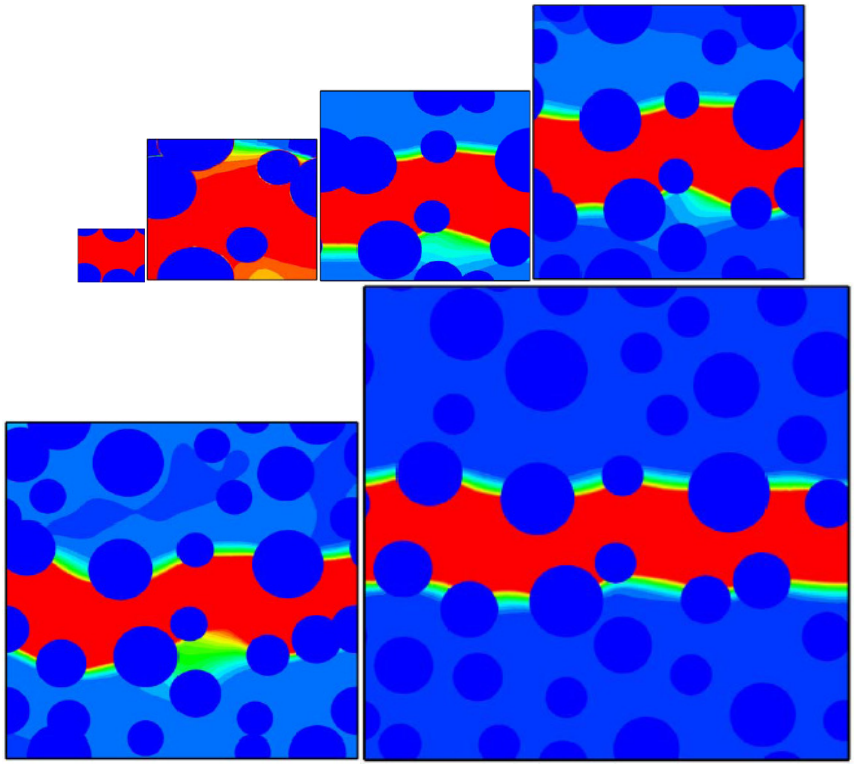

Fig. 9.54 Distribution of non-local softening strain measure for various specimen sizes and stress-strain curves of Fig. 9.53a using standard averaging procedure (characteristic length l_c=1.5 mm, aggregate density ρ=30%) (Skarżyński and Tejchman 2012)

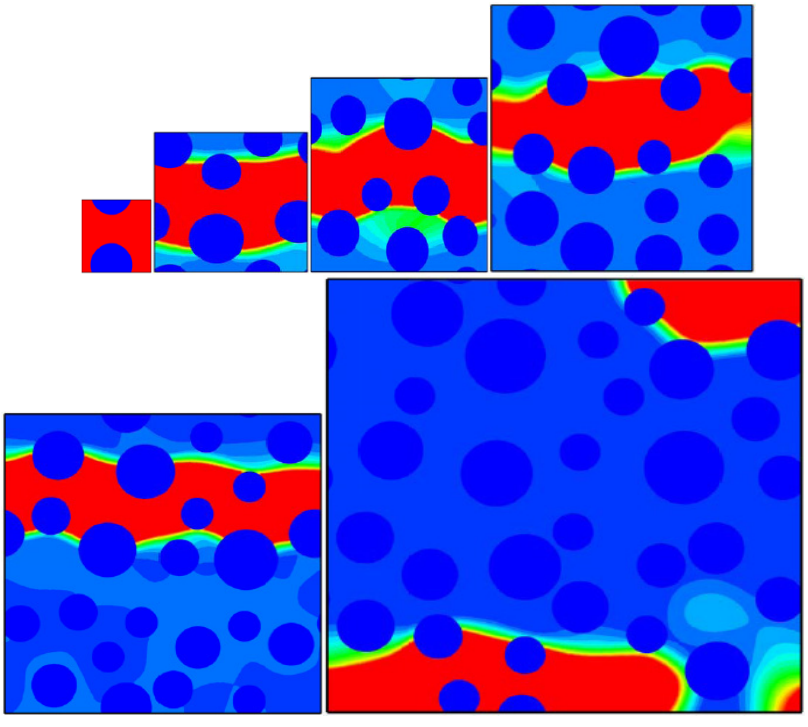

Fig. 9.55 Distribution of non-local softening strain measure for various specimen sizes and stress-strain curves of Fig. 9.53b using standard averaging procedure (characteristic length l_c=1.5 mm, aggregate density ρ=30%) (Skarżyński and Tejchman 2012)

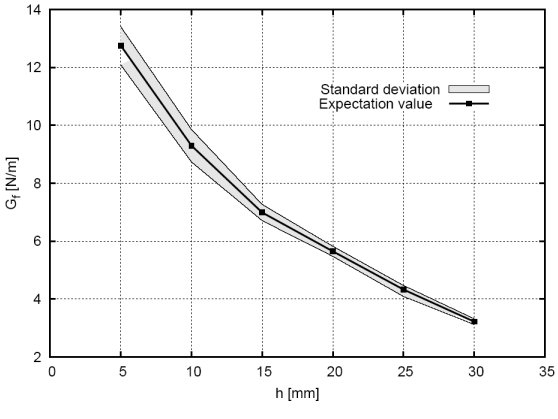

Fig. 9.56 Expected value and standard deviation of tensile fracture energy G_f versus specimen height h using standard averaging (aggregate density ρ=30%) (Skarżyński and Tejchman 2012)

Localized zone averaging approach

Recently, the existence of RVE for softening materials was proved (based on Hill's averaging principle) for cohesive and adhesive failure by deriving a traction-separation law (for a macro crack) instead of a stress-strain relation from microscopic stresses and strains (Verhoosel et al. 2010a, 2010b). This was indicated by the uniqueness (regardless of a micro sample size) of a macro traction-separation law which was obtained by averaging responses along propagating micro discrete cracks. Prompted by this approach and the fact that a localized zone does not scale with the micro specimen size, Nguyen et al. (2010) proposed an approach where homogenized stress and strain were averaged over a localized strain domain in softening materials rather (which is small compared with the specimen size) than over the entire specimen. We used this method in this paper. In this approach, the homogenized stress and strain are

$$<\sigma>=\frac{1}{A_z}\int_{Az}\sigma_m dA_z \qquad \text{and} \qquad <\varepsilon>=\frac{1}{A_z}\int_{A_z}\varepsilon_m dA_z\,, \tag{9.5}$$

where A_z is the localized zone area and σ_m and ε_m are the meso-stress and meso-strain, respectively. The localized zone area A_z is determined on the basis of a distribution of the non-local equivalent strain measure $\bar{\varepsilon}$. As the cut-off value $\bar{\varepsilon}_{\min}=0.005$ is always assumed at the maximum mid-point value usually equal to $\bar{\varepsilon}_{\max}=0.007-0.011$. Thus, a linear material behaviour is simply swept out (which causes the standard stress-strain diagrams to be specimen size dependent), and an active material plastic response is solely taken into account.

Figure 9.57 presents the stress-strain relationships for various specimen sizes and two random aggregate distributions with the material constants from Tab. 9.5 (l_c=1.5 mm) for the calculated localized zones of Figs. 9.54 and 9.55. These stress-strain curves in a softening regime (for the unit cells larger than 10×10 mm^2) are in very good accordance with respect to their shape. In this case, the statistically representative volume element exists and is equal to 15×15 mm^2.

Figure 9.58 presents the expectation value and standard deviation of the tensile fracture energy G_f versus the specimen height h for 3 different realizations. The integration limits were a_1=0 and a_2=0.004. The fracture energy decreases with increasing specimen size approaching an asymptote when the cell size is 15×15 mm^2. Thus, the homogenized stress-strain relationships obtained are objective with respect to the micro sample size. RVE does not represent the entire material in its classical meaning, but the material in a localized zone.

Varying characteristic length approach

With increasing characteristic length, both specimen strength and width of a localized zone increase. On the other hand, softening decreases and material behaves more ductile. Taking these two facts into account, a varying characteristic

length related to the reference specimen size (assumed as 15×15 mm^2 or 30×30 mm^2) is introduced (to scale the width of a localized zone with varying specimen height) according to the formula

$$l^v{}_c = l_c^{15\times15} \times \frac{h}{15} \frac{[\text{mm}]}{[\text{mm}]} \tag{9.6}$$

or

$$l^v{}_c = l_c^{30\times30} \times \frac{h}{30} \frac{[\text{mm}]}{[\text{mm}]}, \tag{9.7}$$

where $l_c^{15\times15}=l_c^{30\times30}=1.5$ mm is a characteristic length for the reference unit cell 15×15 mm^2 or 30×30 mm^2 and h is the unit cell height. A larger unit cell than 30×30 mm^2 can be also used (the width of a localized zone in the reference unit cell cannot be too strongly influenced by boundary conditions, as e.g.. the cell size smaller than 10×10 mm^2). The characteristic length $l^v{}_c$ is no longer a physical parameter related to non-local interactions in the damaging material, but an artificial parameter adjusted to the specimen size.

The stress-strain relationships for various specimen sizes and various characteristic lengths are shown in Figs. 9.59 and 9.60. A characteristic length varies between l_c=0.5 mm for the unit cell 5×5 mm^2 and l_c=3.0 mm for the unit cell 30×30 mm^2 according to Eq. 9.6, and between l_c=0.25 mm for the unit cell 5×5 mm^2 and l_c=1.5 mm for the unit cell 30×30 mm^2 according to Eq. 9.7. The width of a calculated localized zone (for the reference unit cell 15×15 mm^2) is approximately w_c=2 mm=4×l_c=8×s_{cm} (cell 5×5 mm^2), w_c=4 mm=4×l_c=16×s_{cm} (cell 10×10 mm^2), w_c=6 mm=4×l_c=24×s_{cm} (cell 15×15 mm^2), w_c=8 mm=4×l_c=32×s_{cm} (cell 20×20 mm^2), w_c=10 mm=4×l_c=40×s_{cm} (cell 25×25 mm^2) and w_c=12 mm=4×l_c=48×s_{cm} (cell 30×30 mm^2) (Figs. 9.61 and 9.62). The width of a calculated localized zone (for the reference unit cell 30×30 mm^2) is approximately w_c=1 mm=4×l_c=4×s_{cm} (cell 5×5 mm^2), w_c=2 mm=4×l_c=8×s_{cm} (cell 10×10 mm^2), w_c=3 mm=4×l_c=12×s_{cm} (cell 15×15 mm^2), w_c=4 mm=4×l_c=16×s_{cm} (cell 20×20 mm^2), w_c=5 mm=4×l_c=20×s_{cm} (cell 25×25 mm^2) and w_c=6 mm=4×l_c=24×s_{cm} (cell 30×30 mm^2) (Figs. 9.63 and 9.64). A localized zone is scaled with the specimen size. Owing to that the material does not lose its homogeneity and its response during softening is similar for the cell 15×15 mm^2 and larger ones. Thus, the size of the representative volume element is again equal to 15×15 mm^2.

The expected value and standard deviation of the unit fracture energy g_f=G_f/w_c versus the specimen height h are demonstrated in Fig. 9.65. With increasing cell size, the value of g_f stabilizes for the unit cell of 15×15 mm^2.

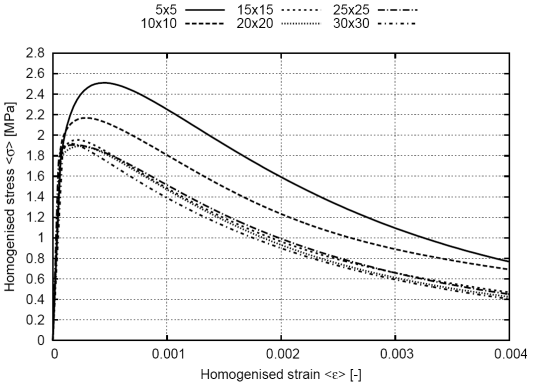

a)

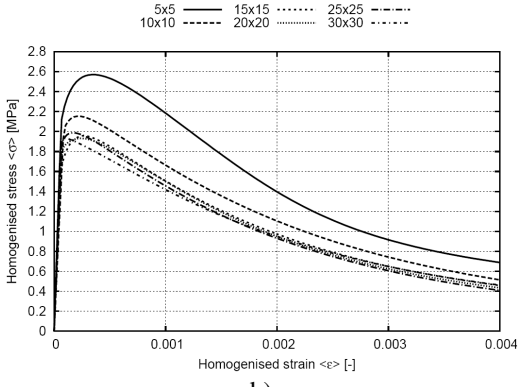

b)

Fig. 9.57 Stress-strain curves for various sizes of concrete specimens and two different random distributions of aggregate (a) and (b) using localized zone averaging procedure (characteristic length l_c=1.5 mm, aggregate density ρ=30%) (Skarżyński and Tejchman 2012)

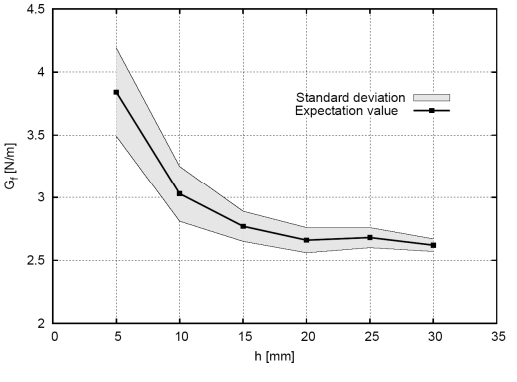

Fig. 9.58 Expected value and standard deviation of tensile fracture energy G_f versus specimen height h using localized zone averaging (aggregate density ρ=30%) (Skarżyński and Tejchman 2012)

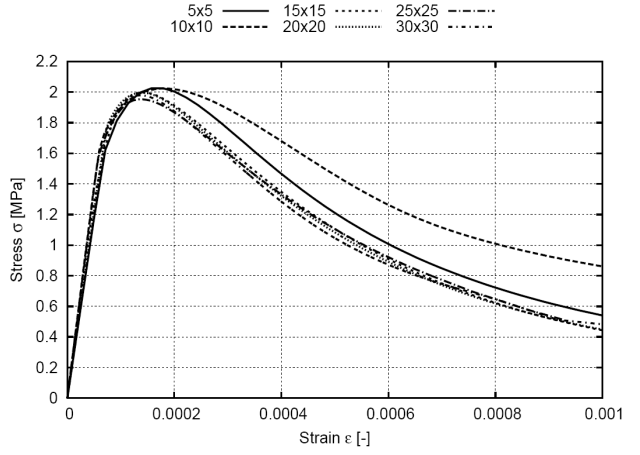

a)

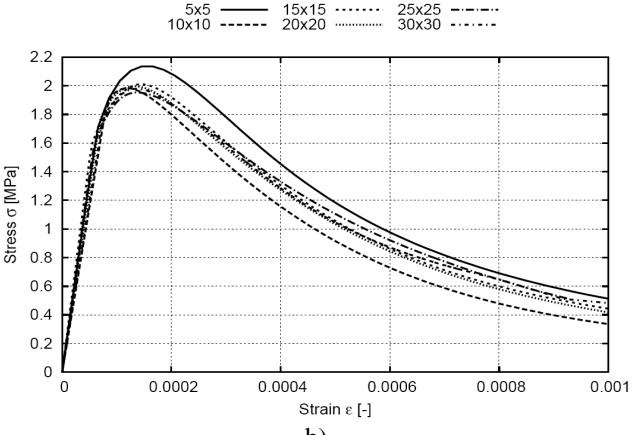

b)

Fig. 9.59 Stress-strain curves for various sizes of concrete specimens and two different random distributions of aggregate (a) and (b) using varying characteristic length approach (reference unit size 15×15 mm^2, characteristic length according to Eq. 9.6, aggregate density ρ=30%) (Skarżyński and Tejchman 2012)

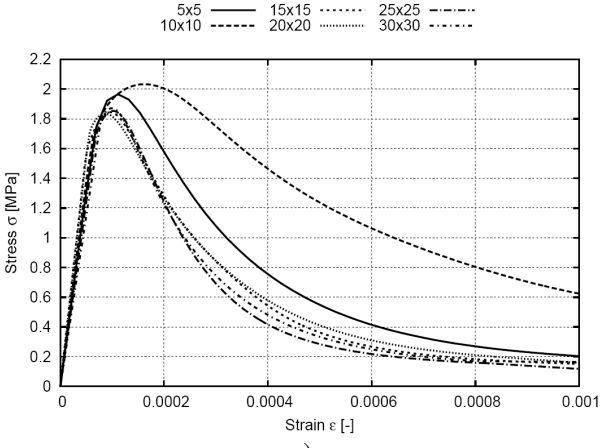

a)

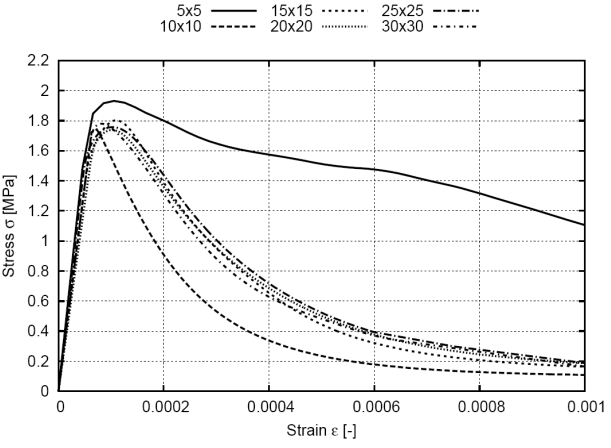

b)

Fig. 9.60 Stress-strain curves for various sizes of concrete specimens and two different random distributions of aggregate (a) and (b) using varying characteristic length approach (reference unit size 30×30 mm^2, characteristic length according to Eq. 9.7, aggregate density ρ=30%) (Skarżyński and Tejchman 2012)

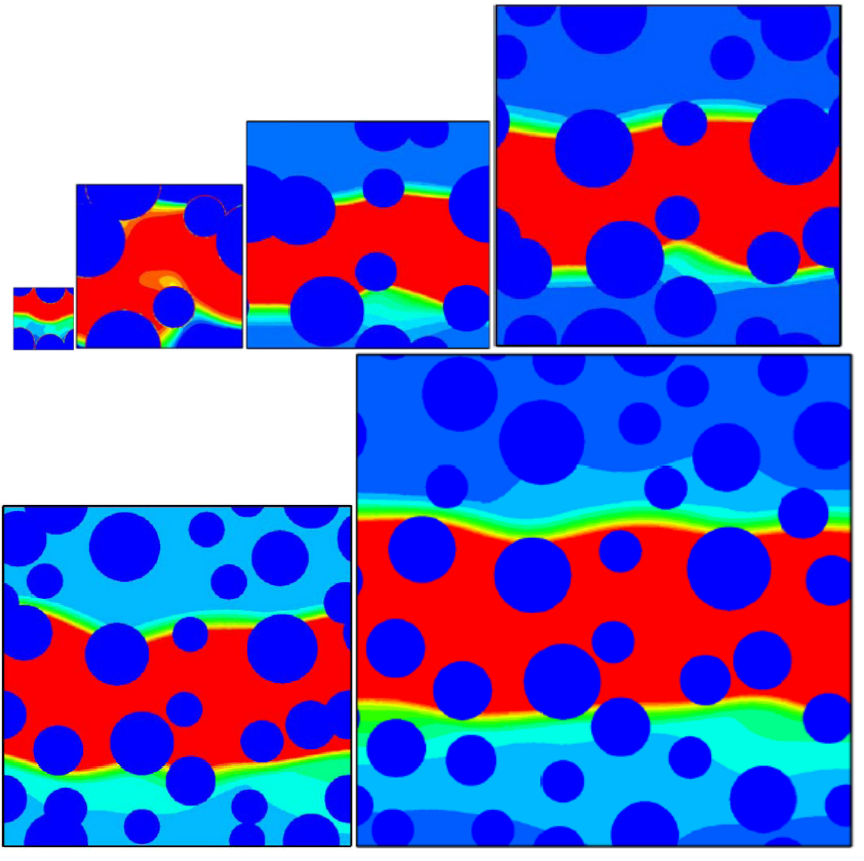

Fig. 9.61 Distribution of non-local softening strain measure for various specimen sizes and stress-strain curves from Fig. 9.59a using varying characteristic length approach (reference unit size 15×15 mm^2, characteristic length according to Eq. 9.6, aggregate density ρ=30%) (Skarżyński and Tejchman 2012)

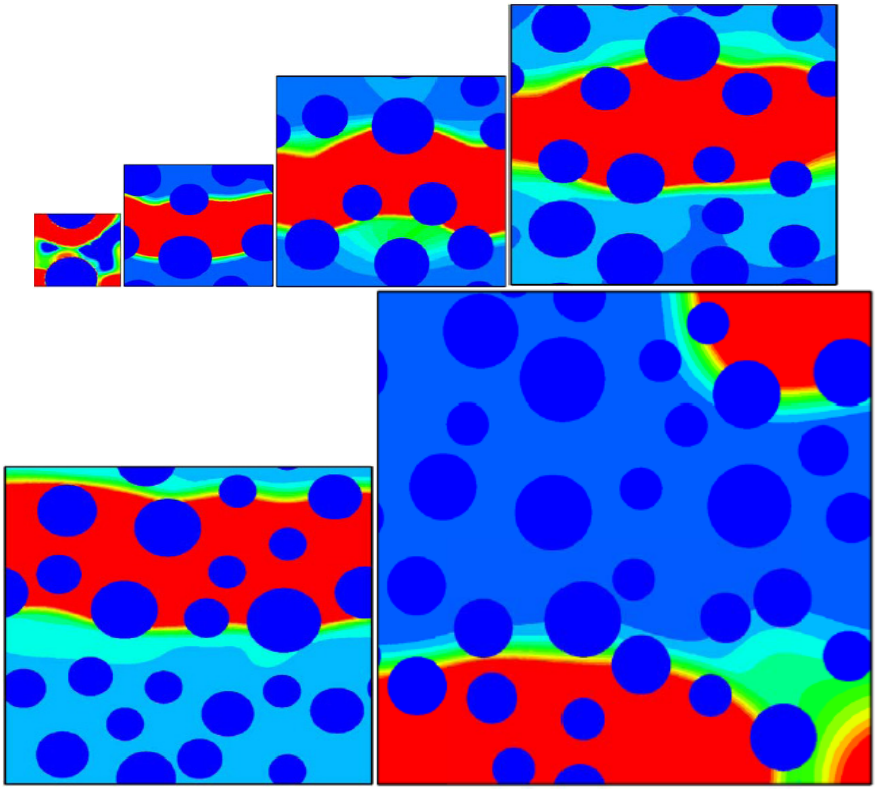

Fig. 9.62 Distribution of non-local softening strain measure for various specimen sizes and stress-strain curves from Fig. 9.59b using varying characteristic length approach (reference unit size 15×15 mm^2, characteristic length according to Eq. 9.6, aggregate density ρ=30%) (Skarżyński and Tejchman 2012)

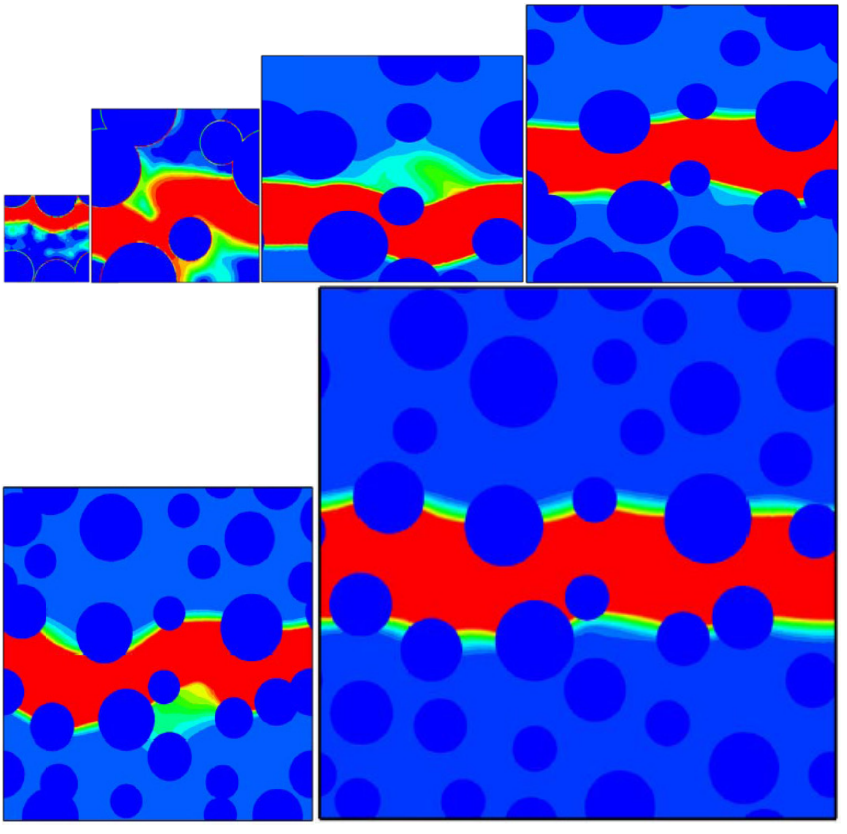

Fig. 9.63 Distribution of non-local softening strain measure for various specimen sizes and stress-strain curves from Fig. 9.60a using varying characteristic length approach (reference unit size 30×30 mm^2, characteristic length according to Eq. 9.7, aggregate density ρ=30%) (Skarżyński and Tejchman 2012)

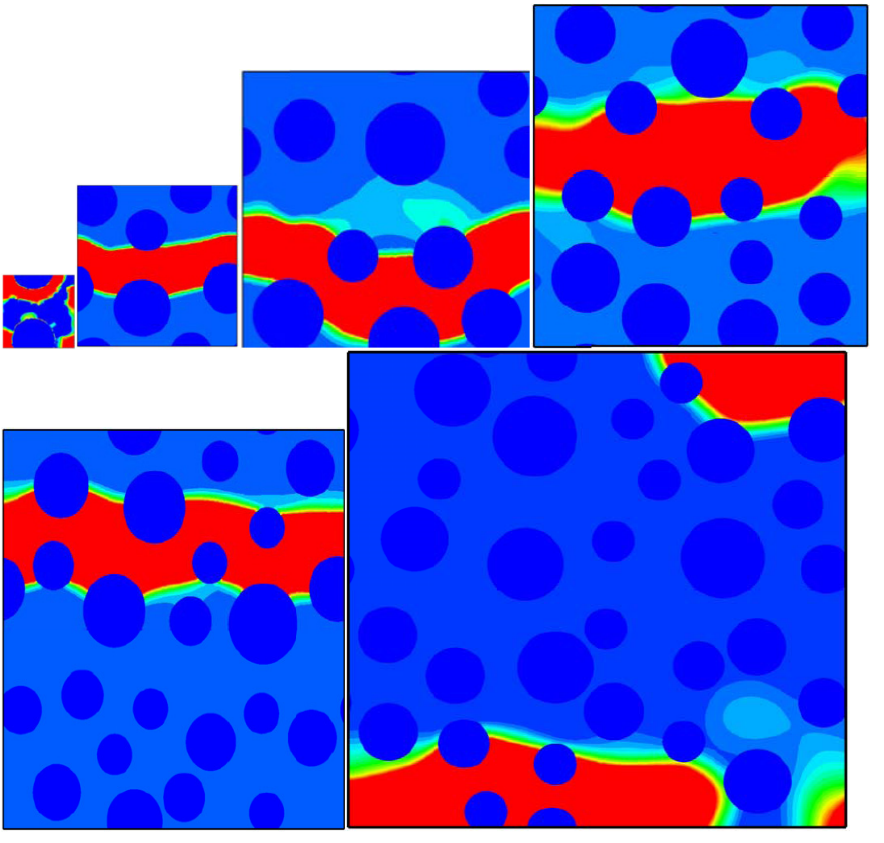

Fig. 9.64 Distribution of non-local softening strain measure for various specimen sizes and stress-strain curves from Fig. 9.60b using varying characteristic length approach (reference unit size 30×30 mm^2, characteristic length according to Eq. 9.7, aggregate density ρ=30%) (Skarżyński and Tejchman 2012)

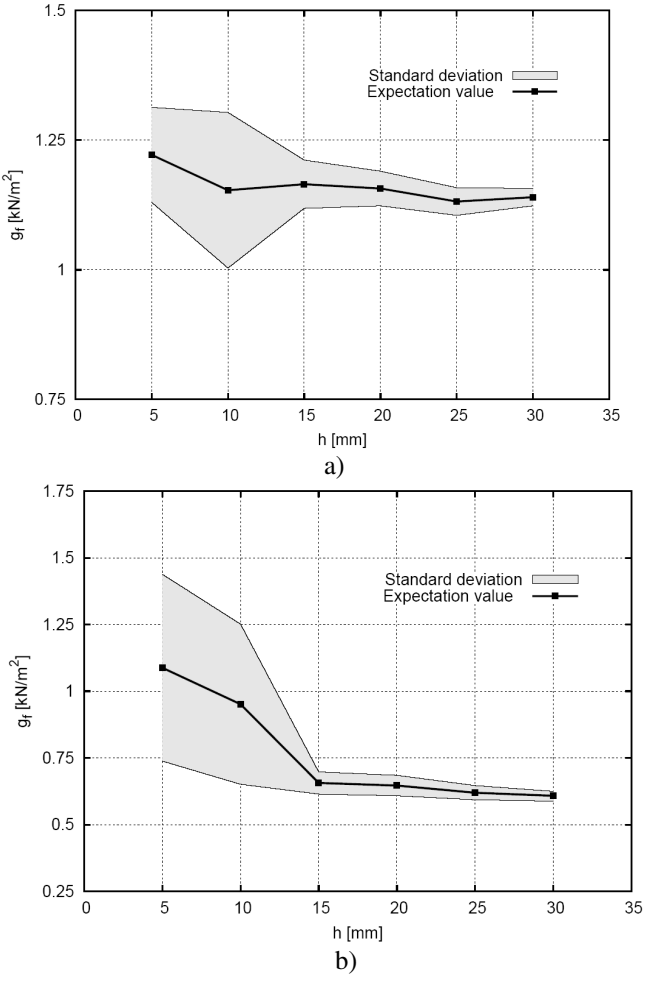

Fig. 9.65 Expected value and standard deviation of unit fracture energy g_f versus specimen height h using varying characteristic length approach: a) reference cell size 15×15 mm^2, b) reference cell size 30×30 mm^2 (aggregate density ρ=30%) (Skarżyński and Tejchman 2012)

The following conclusions can be drawn from our mesoscopic non-linear FE-investigations of strain localization in concrete under tensile loading:

- The 2D representative volume element (RVE) can be determined in quasi-brittle materials using both a localized zone averaging approach and a varying characteristic length approach. In the first case, the averaging is performed over the localized domain rather than over the entire domain, by which the material contribution is swept out. In the second case, the averaging is performed over the entire domain with a characteristic length of micro-structure being scaled with the specimen size. In both cases, convergence of the stress-strain diagrams

for different RVE sizes of a softening material is obtained for tensile loading. The size of a two-dimensional statistically representative volume element is approximately equal to 15×15 mm^2.

- An isotropic continuum damage model with non-local softening is able to capture the mechanism of evolution of strain localization in concrete under tensile loading treated at the meso-scale as a heterogeneous three-phase material.
- Material micro-structure on the meso-scale has to be taken into account in calculations of strain localization to obtain a proper shape of a localized zone.
- The representative volume element (RVE) cannot be defined in quasi-brittle materials with a standard averaging approach (over the entire material domain) due to occurrence of a localized zone whose width is not scaled with the specimen size. The shape of the stress-strain curve depends on the specimen size beyond the elastic region. RVE can be found in homogeneous materials only.
- The 2D representative volume element (RVE) can be determined in quasi-brittle materials using both a localized zone averaging approach and a varying characteristic length approach. In the first case, the averaging is performed over the localized domain rather than over the entire domain, by which the material contribution is swept out. In the second case, the averaging is performed over the entire domain with a characteristic length of micro-structure being scaled with the specimen size. In both cases, convergence of the stress-strain diagrams for different RVE sizes of a softening material is obtained for tensile loading. The size of a two-dimensional statistically representative volume element is approximately equal to 15×15 mm^2.
- The calculated strength, width and geometry of the localized zone are in a satisfactory agreement with experimental measurements when a characteristic length is about 1.5 mm.
- The load-displacement evolutions strongly depend on material parameters assumed for separated concrete phases and a statistical distribution of aggregate. The ultimate beam strength certainly increases with increasing characteristic length, aggregate stiffness, mean aggregate size and decreasing ITZ thickness. It may increase with increasing volume fraction of aggregate. It is also dependent upon aggregate shape.
- Tensile damage is initiated first in the ITZ region. This region is found to have a significant impact on the fracture behaviour and strength of concrete.
- The width of a localized zone increases with increasing characteristic length and decreasing aggregate volume. It may increase if it propagates through weak grains. It is not affected by the aggregate size, aggregate shape, stochastic distribution, ITZ thickness and notch size. The width of a calculated localized zone above the notch changes from about $2\times l_c$ (ρ=60%) up to $4\times l_c$ (ρ=30%) at l_c=1.5 mm. If l_c=5 mm, the width of a calculated localized zone above the notch changes from $2.8\times l_c$ (ρ=60%) up to $3.5\times l_c$ (ρ=30%).
- The calculated increment rate of the width of a localized zone is similar as in experiments.

- Concrete softening is strongly influenced by the statistical distribution of aggregate, characteristic length, volume fraction of aggregate, aggregate shape, aggregate stiffness and ITZ thickness.
- Beams strength increases with increasing characteristic length, aggregate density and aggregate roughness and decreasing beam height. It depends also on the aggregate distribution.
- The localized zone above the notch is strongly curved with l_c=1.0-2.5 mm.

The mesoscopic modelling allows for a better understanding of the mechanism of strain localization. However, it cannot be used for engineering problems due to a long computation time and too small knowledge on both properties of meso-phases in concrete and a stochastic distribution of aggregate which are of a major importance. A direct link between a characteristic length and material micro-structure remains still open. To realistically describe the entire fracture process in concrete, a combined continuous-discontinuous numerical approach has to be used.

References

Bažant, Z.P., Novak, D.: Stochastic models for deformation and failure of quasibrittle structures: recent advances and new directions. In: Bicanić, N., de Borst, R., Mang, H., Meschke, G. (eds.) Computational Modelling of Concrete Structures, pp. 583–598 (2003)

Bažant, Z.P., Oh, B.H.: Crack band theory for fracture of concrete. Materials and Structures RILEM 16(93), 155–177 (1983)

Bažant, Z.P., Pijauder-Cabot, G.: Measurement of characteristic length of non-local continuum. ASCE Journal of Engineering Mechanics 115(4), 755–767 (1989)

Bažant, Z., Planas, J.: Fracture and size effect in concrete and other quasi-brittle materials. CRC Press LLC (1998)

Belytschko, T., Moes, N., Usui, S., Parimi, C.: Arbitrary discontinuities in finite elements. International Journal for Numerical Methods in Engineering 50(4), 993–1013 (2001)

Belytschko, T., Gracie, R., Ventura, G.: A review of extended/generalized finite element methods for material modeling. Modelling and Simulation in Material Science and Engineering 17(4), 1–24 (2009)

Bobiński, J., Tejchman, J.: Numerical simulations of localization of deformation in quasi-brittle materials with non-local softening plasticity. Computers and Concrete 1(4), 433–455 (2004)

Carol, I., López, C.M., Roa, O.: Micromechanical analysis of quasi-brittle materials using fracture-based interface elements. International Journal for Numerical Methods in Engineering 52(12), 193–215 (2001)

Donze, F.V., Magnier, S.A., Daudeville, L., Mariotti, C.: Numerical study of compressive behaviour of concrete at high strain rates. Journal for Engineering Mechanics 125(10), 1154–1163 (1999)

Drugan, W.J., Willis, J.R.: A micromechanics-based nonlocal constitutive equations and estimates of representative volume element size for elastic composites. Journal of the Mechanics and Physics of Solids 44(4), 497–524 (1996)

Du, C.B., Sun, L.G.: Numerical simulation of aggregate shapes of two dimensional concrete and its application. Journal of Aerospace Engineering 20(3), 172–178 (2007)

Eckardt, S., Konke, C.: Simulation of damage in concrete structures using multi-scale models. In: Bicanić, N., de Borst, R., Mang, H., Meschke, G. (eds.) Computational Modelling of Concrete Structures, EURO-C, pp. 77–89. Taylor and Francis (2006)

Evesque, P.: Fluctuations, correlations and representative elementary volume (REV) in granular materials. Poudres et Grains 11(1), 6–17 (2000)

Geers, M.G.D., Kouznetsova, V.G., Brekelmans, W.A.M.: Multi-scale computational homogenization: trends and challenges. Journal of Computational and Applied Mathematics 234(7), 2175–2182 (2010)

Gitman, I.M.: Representative Volumes and multi-scale modelling of quasi-brittle materials, PhD Thesis. Delft University of Technology (2006)

Gitman, I.M., Askes, H., Sluys, L.J.: Representative volume: existence and size determination. Engineering Fracture Mechanics 74(16), 2518–2534 (2007)

Gitman, I.M., Askes, H., Sluys, L.J.: Coupled-volume multi-scale modelling of quasi-brittle material. European Journal of Mechanics A/Solids 27(3), 302–327 (2008)

He, H., Guo, Z., Stroeven, P., Stroeven, M., Sluys, L.J.: Influence of particle packing on elastic properties of concrete. In: Proc. First International Conference on Computational Technologies in Concrete Structures (CTCS 2009), Jeju, Korea, pp. 1177–1197 (2009)

He, H.: Computational modeling of particle packing in concrete. PhD Thesis. Delft University of Technology (2010)

Hill, R.: Elastic properties of reinforced solids: some theoretical principles. Journal of the Mechanics and Physics of Solids 11(5), 357–372 (1963)

Kaczmarczyk, L., Pearce, C.J., Bicanic, N., de Souza Neto, E.: Numerical multiscale solution strategy for fracturing heterogeneous materials. Computer Merhods in Applied Mechanics and Engineering 199(17-20), 1100–1113 (2010)

Kanit, T., Forest, S., Galliet, I., Mounoury, V., Jeulin, D.: Determination of the size of the representative volume element for random composites: statistical and numerical approach. International Journal of Solids and Structures 40(13-14), 3647–3679 (2003)

Kim, S.M., Abu Al-Rub, R.K.: Meso-scale computational modelling of the plastic-damage response of cementitious composites. Cement and Concrete Research 41(3), 339–358 (2011)

Kouznetsova, V.G., Geers, M.G.D., Brekelmans, W.A.M.: Size of Representative Volume Element in a second-order computational homogenization framework. International Journal for Multiscale Computational Engineering 2(4), 575–598 (2004)

Kozicki, J., Tejchman, J.: Modeling of fracture processes in concrete using a novel lattice model. Granular Matter 10(5), 377–388 (2008)

Le Bellĕgo, C., Dube, J.F., Pijaudier-Cabot, G., Gerard, B.: Calibration of nonlocal damage model from size effect tests. European Journal of Mechanics A/Solids 22(1), 33–46 (2003)

Lilliu, G., van Mier, J.G.M.: 3D lattice type fracture model for concrete. Engineering Fracture Mechanics 70(7-8), 927–941 (2003)

Marzec, I., Bobiński, J., Tejchman, J.: Simulations of crack spacing in reinforced concrete beams using elastic-plastic and damage with non-local softening. Computers and Concrete 4(5), 377–403 (2007)

Mihashi, H., Nomura, N.: Correlation between characteristics of fracture process zone and tension softening properties of concrete. Nuclear Engineering and Design 165(3), 359–376 (1996)

Nguyen, V.P., Lloberas Valls, O., Stroeven, M., Sluys, L.J.: On the existence of representative volumes for softening quasi-brittle materials. Computer Methods in Applied Mechanics and Engineering 199(45-48), 3028–3038 (2010)

Nielsen, A.U., Montiero, P.J.M., Gjorv, O.E.: Estimation of the elastic moduli of lightweight aggregate. Cement and Concrete Research 25(2), 276–280 (1995)

Pijaudier-Cabot, G., Bažant, Z.P.: Nonlocal damage theory. Journal of Engineering Mechanics ASCE 113(10), 1512–1533 (1987)

Sengul, O., Tasdemir, C., Tasdemir, M.A.: Influence of aggregate type on mechanical behaviour of normal- and high-strength concretes. ACI Materials Journal 99(6), 528–533 (2002)

Shahbeyk, S., Hosseini, M., Yaghoobi, M.: Mesoscale finite element prediction of concrete failure. Computational Materials Science 50(7), 1973–1990 (2011)

Skarżyński, L., Tejchman, J.: Mescopic modeling of strain localization in concrete. Archives of Civil Engineering LV(4), 521–540 (2009)

Skarżyński, L., Tejchman, J.: Calculations of fracture process zones on meso-scale in notched. concrete beams subjected to three-point bending. European Journal of Mechanics A/Solids 29(4), 746–760 (2010)

Skarżynski, L., Syroka, E., Tejchman, J.: Measurements and calculations of the width of the fracture process zones on the surface of notched concrete beams. Strain 47(s1), 319–322 (2011)

Skarżyński, L., Tejchman, J.: Determination of representative volume element in concrete under tensile deformation. Computers and Concrete 1(9), 35–50 (2012)

Syroka, E., Tejchman, J.: Experimental investigations of size effect in reinforced concrete beams without shear reinforcement. Internal Report. Gdańsk University of Technology (2011)

van der Sluis, O.: Homogenisation of structured elastoviscoplastic solids. PhD Thesis. Technical University Eindhoven (2001)

van Mier, J.G.M., Schlangen, E., Vervuurt, A.: Latice type fracture models for concrete. In: Mühlhaus, H.-B. (ed.) Continuum Models for Material and Microstructure, pp. 341–377. John Wiley & Sons (1995)

van Mier, J.G.M.: Microstructural effects on fracture scaling in concrete, rock and ice. In: Dempsey, J.P., Shen, H.H. (eds.) IUTAM Symposium on Scaling Laws in Ice Mechanics and Ice Dynamics, pp. 171–182. Kluwer Academic Publishers (2000)

Verhoosel, C.V., Remmers, J.J.C., Gutierrez, M.A.: A partition of unity-based multiscale approach for modelling fracture in piezoelectric ceramics. International Journal for Numerical Methods in Engineering 82(8), 966–994 (2010a)

Verhoosel, C.V., Remmers, J.J.C., Gutieerrez, M.A., de Borst, R.: Computational homogenization for adhesive and cohesive failure in quasi-brittle solids. International Journal for Numerical Methods in Engineering 83(8-9), 1155–1179 (2010b)

White, D.J., Take, W.A., Bolton, M.D.: Soil deformation measurement using particle image velocimetry (PIV) and photogrammetry. Geotechnique 53(7), 619–631 (2003)